

Exploring how groundwater buffers the influence of heatwaves on vegetation function during multi-year droughts

Mengyuan Mu¹, Martin G. De Kauwe^{1,2}, Anna M. Ukkola¹, Andy J. Pitman¹, Weidong Guo³, Sanaa Hobeichi¹, Peter R. Briggs⁴

¹ARC Centre of Excellence for Climate Extremes and Climate Change Research Centre, University of New South Wales, Sydney 2052, Australia

²School of Biological Sciences, University of Bristol, Bristol BS8 1TQ, United Kingdom

³School of Atmospheric Sciences and Joint International Research Laboratory of Atmospheric and Earth System Sciences, Nanjing University, Nanjing 210023, China

⁴Climate Science Centre, CSIRO Oceans and Atmosphere, Canberra 2601, ACT, Australia

Correspondence to: Mengyuan Mu (mu.mengyuan815@gmail.com)

Abstract. The co-occurrence of droughts and heatwaves can have significant impacts on many socioeconomic and environmental systems. Groundwater has the potential to moderate the impact of droughts and heatwaves by moistening the soil and enabling vegetation to maintain higher evaporation, thereby cooling the canopy. We use the Community Atmosphere Biosphere Land Exchange (CABLE) land surface model, coupled to a groundwater scheme, to examine how groundwater influences ecosystems under conditions of co-occurring droughts and heatwaves. We focus specifically on South East Australia for the period 2000–2019 when two significant droughts and multiple extreme heatwave events occurred. We found groundwater plays an important role in helping vegetation maintain transpiration, particularly in the first 1–2 years of a multi-year drought. Groundwater impedes gravity-driven drainage and moistens the root zone via capillary rise. These mechanisms reduced forest canopy temperatures by up to 5°C during individual heatwaves, particularly where the water table depth is shallow. The role of groundwater diminishes as the drought lengthens beyond 2 years and soil water reserves are depleted. Further, the lack of deep roots or stomatal closure caused by high vapour pressure deficit or high temperatures can reduce the additional transpiration induced by groundwater. The capacity of groundwater to moderate both water and heat stress on ecosystems during simultaneous droughts and heatwaves is not represented in most global climate models, suggesting model projections may overestimate the risk of these events in the future.

1 Introduction

Droughts and heatwaves are important socio-economic and environmental phenomena, impacting regional food production (Kim et al., 2019; Lesk et al., 2016), water resources (Leblanc et al., 2009; Orth and Destouni, 2018) and the resilience of ecosystems (Ibáñez et al., 2019; Ruehr et al., 2019; Sandi et al., 2020). When droughts and heatwaves co-occur (a “compound event”) the consequences can be particularly severe, reducing the terrestrial carbon sink (Ciais et al., 2005), potentially accelerating tree die-off (Allen et al., 2010, 2015; Birami et al., 2018) and setting conditions conducive for wildfires (Jyoteeshkumar reddy et al., 2021). One region experiencing severe coincident heatwaves and drought is Australia (Mitchell et al., 2014). Drought in Australia is associated with large-scale modes of variability, including the El Niño-Southern Oscillation and the Indian Ocean Dipole (van Dijk et al., 2013), and periods of below average rainfall can extend for multiple years (Verdon-Kidd and Kiem, 2009). Heatwaves are commonly synoptically driven, associated with blocking events that can be sustained over many days (Perkins-Kirkpatrick et al., 2016; Perkins, 2015). Modes of variability and synoptic situations are important in setting up conditions conducive to drought and heatwave. However, once a heatwave or drought has become established, land-atmosphere interactions can intensify and prolong both heatwaves and droughts (Miralles et al., 2019), affect their intensity and influence the risk of their co-occurrence (Mukherjee et al., 2020). The role of the land surface in amplifying or dampening heatwaves and droughts is associated with the partitioning of available energy between sensible and latent heat (Fischer et al.,

41 2007; Hirsch et al., 2019) and is regulated by sub-surface water availability (Teuling et al., 2013; Zhou et al., 2019). As soil
42 moisture becomes more limiting, more of the available energy is converted into sensible heat, reducing evaporative cooling via
43 latent heat. Changes in the surface turbulent energy fluxes influence the humidity in the boundary layer, the formation of clouds,
44 incoming solar radiation and the generation of rainfall (D'Odorico and Porporato, 2004; Seneviratne et al., 2010; Zhou et al.,
45 2019). The sensible heat fluxes warm the boundary layer, leading to heat that can accumulate over several days and exacerbate
46 heat extremes (Miralles et al., 2014), which can in turn increase the atmospheric demand for water and intensify drought
47 (Miralles et al., 2019; Schumacher et al., 2019).

48

49 Vegetation access to groundwater has the potential to alter these land-atmosphere feedbacks by maintaining vegetation function
50 during extended dry periods, supporting transpiration and moderating the impact of droughts and heatwaves (Marchionni et al.,
51 2020; Miller et al., 2010). Where the water table is relatively shallow, capillarity may bring water from the groundwater towards
52 the surface root zone, increasing plant water availability. Where the water table is deeper, phreatophytic vegetation with tap
53 roots can directly access groundwater (Zencich et al., 2002). The presence of groundwater, and the access to groundwater by
54 vegetation is therefore likely to buffer vegetation drought and heatwave stress. For example, groundwater may help vegetation
55 sustain transpiration and consequently cool plant canopies via evaporation. This is particularly critical during compound events
56 where cessation of transpiration would increase the risk of impaired physiological function and the likelihood that plants would
57 exceed thermal limits and risk mortality (Geange et al., 2021; O'sullivan et al., 2017; Sandi et al., 2020).

58

59 Quantifying the influence of groundwater on vegetation function has remained challenging as concurrent observations of
60 groundwater dynamics, soil moisture, and energy and water fluxes are generally lacking over most of Australia and indeed
61 many parts of the world. Land surface models (LSMs) provide an alternative tool for studying the interactions between
62 groundwater, vegetation, and surface fluxes in the context of heatwaves and droughts (Gilbert et al., 2017; Martinez et al., 2016a;
63 Maxwell et al., 2011; Shrestha et al., 2014). However, there has been very little work focused on the influence of groundwater
64 on droughts and heatwaves occurring at the same time (Keune et al., 2016; Zipper et al., 2019). Our key goal in this paper is
65 therefore to examine the timescales and extent to which vegetation utilises groundwater during drought and heatwaves, and
66 determine the degree to which groundwater can mitigate the impacts of compound extremes. We focus on droughts and
67 heatwaves occurring over south-eastern (S.E.) Australia during 2000–2019 using the Community Atmosphere Biosphere Land
68 Exchange (CABLE) LSM. S.E. Australia is an ideal case study since its forest and woodland ecosystems are known to be
69 dependent on groundwater (Eamus and Froend, 2006; Kuginis et al., 2016; Zencich et al., 2002) and it has experienced two
70 multi-year droughts and record-breaking heatwaves over the last two decades. By examining the role of groundwater in
71 influencing droughts and heatwaves, and by understanding how well CABLE can capture the relevant processes, we aim to
72 build confidence in the simulations of land-atmosphere interactions for future droughts and heatwaves.

73 2 Methods

74 2.1 Study area

75 The climate over S.E. Australia varies from humid temperate near the coast to semi-arid in the interior. In the last 20 years, S.E.
76 Australia experienced the 9-year Millennium drought during 2001–2009 (van Dijk et al., 2013) where rainfall dropped from a
77 climatological average (1970–1999) of 542 mm yr^{-1} to 449 mm yr^{-1} , and a 3-year intense recent drought during 2017–2019
78 where rainfall dropped to 354 mm yr^{-1} (Figure S1). It has also suffered record-breaking summer heatwaves in 2009, 2013, 2017,
79 and 2019 (Bureau of Meteorology, 2013, 2017, 2019; National Climate Centre, 2009). Here we investigate groundwater
80 interactions during the period 2000–2019, focusing on the Millennium drought (MD, 2001–2009) and the recent drought (RD,
81 2017–2019).

82 **2.2 Overview of CABLE**

83 CABLE is a process-based LSM that simulates the interactions between climate, plant physiology and hydrology (Wang et al.,
 84 Above ground, CABLE simulates the exchange of carbon, energy and water fluxes, using a single layer, two-leaf
 85 (sunlit/shaded) canopy model (Wang and Leuning, 1998), with a treatment of within-canopy turbulence (Raupach, 1994;
 86 Raupach et al., 1997). CABLE includes a 6-layer soil model (down to 4.6 m) with soil hydraulic and thermal characteristics
 87 dependent on the soil type and soil moisture content. CABLE has been extensively evaluated (e.g., Abramowitz et al., 2008;
 88 Wang et al., 2011; Zhang et al., 2013) and benchmarked (Abramowitz 2012; Best et al. 2015) at global and regional scales.
 89 Here we adopt a version of CABLE (Decker, 2015; Decker et al., 2017) which includes a dynamic groundwater component
 90 with aquifer water storage. This version, CABLE-GW, has been previously evaluated by Decker (2015), Ukkola et al. (2016b)
 91 and Mu et al. (2021) and shown to perform well for simulating water fluxes. CABLE code is freely available upon registration
 92 (<https://trac.nci.org.au/trac/cable/wiki>); here we use CABLE SVN revision 7765.

93 **2.3 Hydrology in CABLE-GW**

94 The hydrology scheme in CABLE-GW solves the vertical redistribution of soil water via a modified Richards equation (Zeng
 95 and Decker, 2009):

96

$$97 \frac{\partial \theta}{\partial t} = -\frac{\partial}{\partial z} K \frac{\partial}{\partial z} (\Psi - \Psi_E) - F_{soil} \quad (1)$$

98

99 where θ is the volumetric water content of the soil ($\text{mm}^3 \text{ mm}^{-3}$), K is the hydraulic conductivity (mm s^{-1}), z is the soil depth
 100 (mm), Ψ and Ψ_E are the soil matric potential (mm) and the equilibrium soil matric potential (mm), and F_{soil} is a sink term
 101 related to subsurface runoff and transpiration (s^{-1}) (Zeng and Decker, 2009; Decker, 2015). To simulate groundwater dynamics,
 102 an unconfined aquifer is added to the bottom of the soil column with a simple water balance model:

103

$$104 \frac{dW_{aq}}{dt} = q_{re} - q_{aq,sub} \quad (2)$$

105

106 where W_{aq} is the mass of water in the aquifer (mm), $q_{aq,sub}$ is the subsurface runoff in the aquifer (mm s^{-1}), and q_{re} is the water
 107 flux between the aquifer and the bottom soil layer (mm s^{-1}) computed by the modified Darcy's law:

108

$$109 q_{re} = \frac{(K_{aq} + K_{bot})}{2} \frac{(\Psi_{aq} - \Psi_n) - (\Psi_{E,aq} - \Psi_{E,n})}{z_{wtd} - z_n} \quad (3)$$

110

111 where K_{aq} and K_{bot} are the hydraulic conductivity in the aquifer and in the bottom soil layer (mm s^{-1}), Ψ_{aq} and $\Psi_{E,aq}$ are the
 112 soil matric potentials for the aquifer (mm), and Ψ_n and $\Psi_{E,n}$ are the soil matric potentials for the bottom soil layer (mm). z_{wtd}
 113 and z_n are the depth of the water table (mm) and the lowest soil layer (mm), respectively. The positive q_{re} refers to the
 114 downward water flow from soil column to aquifer (i.e. vertical drainage, Dr), and the negative q_{re} is the upward water
 115 movement from aquifer to soil column (i.e., recharge, Qrec). CABLE-GW assumes the groundwater aquifer sits above
 116 impermeable bedrock, giving a bottom boundary condition of:

117

$$118 q_{out} = 0 \quad (4)$$

119

120 CABLE-GW computes the subsurface runoff (q_{sub} , mm s^{-1}) using:

121

122 $q_{sub} = \sin \frac{\overline{dz}}{d_l} \hat{q}_{sub} e^{-\frac{z_{wtd}}{f_p}}$ (5)

123

124 where $\frac{\overline{dz}}{d_l}$ is the mean subgrid-scale slope, \hat{q}_{sub} is the maximum rate of subsurface drainage (mm s^{-1}) and f_p is a tunable
125 parameter. q_{sub} is generated from the aquifer and the saturated deep soil layers (below the third soil layer).

126 **2.4 Experiment design**

127 To explore how groundwater influences droughts and heatwaves, we designed two experiments, with and without groundwater
128 dynamics, driven by the same 3-hour time-evolving meteorology forcing and the same land surface properties (see section 2.5
129 for datasets) for the period 1970–2019 at a 0.05° spatial resolution with a 3-hour time step. To correct a tendency for high soil
130 evaporation, we implemented a parameterisation of soil evaporation resistance that has previously been shown to improve the
131 model (Decker et al., 2017; Mu et al., 2021).

132 **2.4.1 Groundwater experiment (GW)**

133 This simulation uses the default CABLE-GW model, which includes the unconfined aquifer to hold the groundwater storage
134 and simulates the water flux between the bottom soil layer and the aquifer. We first ran the default CABLE-GW with fixed CO_2
135 concentrations at 1969 levels for 90 years by looping the time-evolving meteorology forcing over 1970–1999. At the end of the
136 90-year spin-up, moisture in both the soil column and the groundwater aquifer reached an effective equilibrium when averaged
137 over the study area. We then ran the model from 1970 to 2019 with time varying CO_2 . We omit the first 30 years of this period
138 and analyse the period 2000–2019 to allow for further equilibrium with the time-evolving CO_2 .

139 **2.4.2 Free drainage experiment (FD)**

140 Many LSMs, including those used in the Coupled Model Intercomparison Project 5 (CMIP5), still use a free drainage
141 assumption and neglect the parameterisation of the unconfined aquifer. To test the impact of this assumption we decoupled the
142 aquifer from the bottom soil layer and thus removed the influence of groundwater dynamics (experiment FD). In FD, at the
143 interface between the bottom soil layer and the aquifer, soil water can only move downwards as vertical drainage at the rate
144 defined by the bottom soil layer's hydraulic conductivity:

145

146 $q_{re} = K_{bot}$ (6)

147

148 This vertical drainage is added to the subsurface runoff flux:

149

150 $q_{sub} = q_{sub} + q_{re}$ (7)

151

152 The simulated water table depth (WTD, i.e. z_{wtd}) in CABLE-GW affects the water potential gradient between the soil layers
153 via Ψ_E (Zeng and Decker, 2009) and impacts q_{sub} (Equation 5). However, in FD, decoupling the soil column from the aquifer
154 and adding vertical drainage directly to subsurface runoff causes an artificial and unrealistic decline in WTD. To solve this
155 problem, we assume a fixed WTD in the FD simulations at 10 m in order to remove this artefact from the simulation of Ψ_E and
156 q_{sub} .

157

158 The FD simulations are initialised from the near-equilibrated state at the end of the 90-year spin-up used in GW. The period
159 1970–2019 is then simulated using varying CO_2 and the last 20 years are used for analysis.

160 **2.4.3 Deep root experiment (DR)**

161 The parameterisation of roots, including the prescription of root parameters in LSMs, is very uncertain (Arora and Boer, 2003;
 162 Drewniak, 2019) and LSMs commonly employ root distributions that are too shallow (Wang and Dickinson, 2012). The vertical
 163 distribution of roots influences the degree to which plants can utilise groundwater, and potentially the role groundwater plays
 164 in influencing droughts and heatwaves. To explore the uncertainty associated with root distribution, we added a “deep root”
 165 (DR) experiment by increasing the effective rooting depth in CABLE for tree areas. In common with many LSMs, CABLE-
 166 GW defines the root distribution following Gale and Grigal (1987):

$$168 \quad f_{root} = 1 - \beta_{root}^z \quad (8)$$

170 where f_{root} is the cumulative root fraction (between 0 and 1) from the soil surface to depth z (cm), and β_{root} is a fitted parameter
 171 specified for each plant functional type (PFT) (Jackson et al., 1996). In CABLE, the tree areas in our study region are simulated
 172 as evergreen broadleaf PFT (Figure S2a) with a $\beta_{root} = 0.962$, implying that only 8% of the simulated roots are located below
 173 the soil depth of 0.64 m (Figure S2b). However, field observations (Canadell et al., 1996; Eberbach and Burrows, 2006; Fan et
 174 al., 2017; Griffith et al., 2008) suggest that the local trees tend to have a far deeper root system, possibly to help cope with the
 175 high climate variability. We therefore increased β_{root} for the evergreen broadleaf PFT to 0.99, which assumes 56 % of roots
 176 are located in depths below 0.64 m and 21 % of roots below 1.7 m (Figure S2b). This enables the roots to extract larger quantities
 177 of deep soil water moisture, which is more strongly influenced by groundwater.

178 Given we lack the detailed observations to set root distributions across S.E. Australia, we undertake the DR experiment as a
 179 simple sensitivity study. We only run this experiment during January 2019, when the record-breaking heatwaves compound
 180 with the severe recent drought. The DR experiment uses identical meteorology forcing and land surface properties as GW and
 181 FD, and is initialised by the state of the land surface on the 31st December 2018 from the GW experiment.

183 **2.5 Datasets**

184 Our simulations are driven by the atmospheric forcing from the Australian Water Availability Project (AWAP), which provides
 185 daily gridded data covering Australia at 0.05° spatial resolution (Jones et al., 2009). This dataset has been widely used to force
 186 LSMs for analysing the water and carbon balances in Australia (Haverd et al., 2013; De Kauwe et al., 2020; Raupach et al.,
 187 2013; Trudinger et al., 2016). The AWAP forcing data include observed fields of precipitation, solar radiation, minimum and
 188 maximum daily temperatures and vapour pressure at 9 am and 3 pm. Since AWAP forcing does not include wind and air pressure
 189 we adopted the near-surface wind speed data from McVicar et al. (2008) and assume a fixed air pressure of 1000 hPa. Due to
 190 missing observations before 1990, the solar radiation input for 1970–1989 was built from the 1990–1999 daily climatology.
 191 Similarly, wind speeds for 1970–1974 are built from the 30-year climatology from 1975 to 2004. We translated the daily data
 192 into 3-hourly resolution using a weather generator (Haverd et al., 2013).

193 The land surface properties for our simulations are prescribed based on observational datasets. Land cover type is derived from
 194 the National Dynamic Land Cover Data of Australia (DLCD) (<https://www.ga.gov.au/scientific-topics/earth-obs/accessing-satellite-imagery/landcover>). We classify DLCD’s land cover types to five CABLE PFTs: crop (irrigated/rainfed crop, pasture
 195 and sugar DLCD classes), broadleaf evergreen forest (closed/open/scattered/sparse tree), shrub (closed/open/scattered/sparse
 196 shrubs and open/scattered/sparse chenopod shrubs), grassland (open/sparse herbaceous) and barren land (bare areas). We then
 197 resample the DLCD dataset from the 250 m resolution to the 0.05° resolution. The leaf area index (LAI) in CABLE is prescribed
 198 using a monthly climatology derived from the Copernicus Global Land Service product
 199 (<https://land.copernicus.eu/global/products/lai>). The climatology was constructed by first creating a monthly time series by
 200

202 taking the maximum of the 10-daily timesteps each month and then calculating a climatology from the monthly data over the
203 period 1999–2017. The LAI data was resampled from the original 1 km resolution to the 0.05° resolution following De Kauwe
204 et al. (2020). Soil parameters are derived from the soil texture information (sand/clay/silt fraction) from SoilGrids (Hengl et al.,
205 2017) via the pedotransfer functions in Cosby et al. (1984) and resampled from 250 m to 0.05° resolution.
206

207 To evaluate the model simulations, we use monthly total water storage anomaly (TWSA) at 0.5° spatial resolution from the
208 Gravity Recovery and Climate Experiment (GRACE) and GRACE Follow On products (Landerer et al., 2020; Watkins et al.,
209 2015; Wiese et al., 2016, 2018). The RLM06M release is used for February 2002–June 2017 and for June 2018 – December
210 2019. We also use total land evapotranspiration from the 2000–2018 monthly Derived Optimal Linear Combination
211 Evapotranspiration (DOLCE version 2, Hobeichi et al., 2021) at 0.25° resolution, as well as the 2000–2019 daily Global Land
212 Evaporation Amsterdam Model (GLEAM version 3.5, <https://www.gleam.eu/>; Martens et al., 2017; Miralles et al., 2011) at 0.5°
213 spatial resolution. For daytime land surface temperature (LST) we use the Moderate Resolution Imaging Spectroradiometer
214 (MODIS) datasets from Terra and Aqua satellites (products MOD11A1 and MYD11A1, Wan and Li, 1997; Wan 2015a, 2015b)
215 at 1 km spatial resolution. We only consider pixels and time steps identified as good quality (QC flags 0). Only the day-time
216 LST values are used due to the lack of good quality night-time LST data. The Terra overpass occurs at 10 am and Aqua at 2 pm
217 local time. To analyse the compound events in January 2019, we linearly interpolate the 3-hourly model outputs to 2 pm to
218 match the overpass time of the Aqua LST. The GRACE, GLEAM and MODIS datasets were resampled to the AWAP resolution
219 using bilinear interpolation.
220

221 To evaluate model performance during heatwaves, we identify heatwave events using the excess heat factor index (EHF, Nairn
222 and Fawcett, 2014). EHF is calculated using the daily AWAP maximum temperature, as the product of the difference of the
223 previous 3 day mean to the 90th percentile of the 1970–1999 climatology and the difference of the previous 3 day mean to the
224 preceding 30 day mean. A heatwave occurs when the EHF index is greater than 0 for at least three consecutive days. We only
225 focus on summer heatwaves occurring between December and February of the following year.
226

3 Results

3.1 Simulations for the Millennium Drought and the recent drought

228 Previous studies have shown that simulations by LSMs diverge as the soil dries (Ukkola et al., 2016a), associated with
229 systematic biases in evaporative fluxes and soil moisture states in the models (Mu et al., 2021; Swenson and Lawrence, 2014;
230 Trugman et al., 2018). We therefore first evaluate how well CABLE-GW captures the evolution of terrestrial water variability
231 during two recent major droughts.
232

233 Figure 1a shows the total water storage anomaly during 2000–2019 observed by GRACE and simulated in GW and FD. Both
234 GW and FD accurately capture the interannual variability in total water storage for S.E. Australia ($r = 0.96$ in GW, and 0.90 in
235 FD). Both model configurations simulate a decline in TWSA through the first drought period (up to 2009, see Figure S1), the
236 rapid increase in TWSA from 2010 associated with higher rainfall, a decline from around 2012 due to the re-emergence of
237 drought conditions, and the rapid decline during the recent drought after conditions had eased in 2016 (Figure S1). FD
238 underestimates the magnitude of monthly TWSA variance (standard deviation, SD = 37.18 mm) compared to GRACE (47.74
239 mm) or GW (47.67 mm), particularly during the wetter periods (2000, 2011–2016) and the first ~2 years of the droughts (2001–
240 2, 2017–8) (Figure 1a). This underestimation in FD compared to GW is linked with the lack of aquifer water storage in the FD
241 simulations which provides a reservoir of water that changes slowly and has a memory of previous wet/dry climate conditions
242 (Figure 1a).

243 Figure 1b shows the accumulated precipitation (P) minus evapotranspiration (E) over the two drought periods. GW increases
244 the evapotranspiration relative to FD such that the accumulated P–E decreases from about 786 mm to 455 mm during the
245 Millennium drought, which is within the range of DOLCE (460 mm) and GLEAM (97 mm) estimates. A similar result, although
246 over a much shorter period, is also apparent for the recent drought (Figure 1b). The lower P–E in GW suggests that the presence
247 of groundwater storage can alleviate the vegetation water stress during droughts, and reduces the reliance of E on P, indicated
248 by a small reduction in the correlation (r) between E and P from 0.28 in FD to 0.24 in GW for MD, and a reduction from 0.42
249 to 0.37 for RD (Figure 1b). Although the evapotranspiration products display some differences, the GW simulations are closer
250 overall to both the DOLCE and the GLEAM, observational-constrained estimates. The better match of GW than FD to the two
251 evapotranspiration products implies that adding groundwater improves the simulations during droughts, whilst the remaining
252 mismatch would tend to suggest further biases in simulated evapotranspiration arising from multiple sources (e.g., a mis-match
253 in leaf area index, or contributions from the understorey). The difference in E is also demonstrated spatially in Figure S3. During
254 the Millennium drought, the GW simulations show a clear improvement over FD in two aspects. GW shows smaller biases in
255 E along the coast where FD underestimates E strongly (Figure S3b–c). The areas where E is underestimated are also smaller in
256 extent in GW, suggesting that GW overall reduces the dry bias. The magnitude of the bias in GW reaches around 300 mm over
257 small areas of S.E. Australia while in the FD simulations biases are larger, reaching 400 mm over a larger area. Plant
258 photosynthesis assimilation rates are associated with transpiration via stomata conductance. Figure S4 presents the spatial maps
259 of gross primary productivity (GPP) during the two droughts. GW simulations increase carbon uptake by 50–300 g C yr⁻¹,
260 particularly along the coasts (Figure S4c,f). However, since CABLE uses a prescribed LAI and does not simulate any feedback
261 between water availability and plant growth (e.g., defoliation) and its impact on GPP, we only focus on how GW influences
262 evapotranspiration and the surface energy balance in the subsequent sections.

263

264 Overall, Figure 1 and Figure S3 indicates representing groundwater in the model improves the simulation of the inter-annual
265 variability in the terrestrial water cycle and storage, particularly during droughts.

266 **3.2 The role of groundwater in sustaining evapotranspiration during droughts**

267 We next explore the mechanisms by which including groundwater modifies the simulation of evapotranspiration. Figure 2
268 displays the overall influence of groundwater on water fluxes during the recent drought. GW simulates 50–200 mm yr⁻¹ more E
269 over coastal regions where there is high tree cover (Figure 2a; see Figure S2a for land cover). Adding groundwater also increases
270 E in most other regions, although the impact is negligible in many inland and non-forested regions (i.e., west of 145°E). We
271 identified a clear connection between E (Figure 2a) and the simulated WTD in the GW simulations (Figure S5). GW simulates
272 110 mm yr⁻¹ more E when the WTD is shallower than 5 m deep, 22 mm yr⁻¹ when the WTD is 5–10 m deep, but only 3 mm yr⁻¹
273 more when the WTD is below 10 m. Higher transpiration (Et) in GW explains 78% of the evapotranspiration difference
274 between GW and FD where WTD is shallower than 5 m (Figure 2b). This is confirmed by the change in the soil evaporation
275 (Δ Es) (Figure 2c) where adding groundwater increases Es by negligible amounts over most of S.E. Australia, but by up to 25
276 mm yr⁻¹ in regions underlain by shallow groundwater (Figure S5), which is consistent with field observations that indicate that
277 Es can be substantial under conditions of a very shallow water table (Thorburn et al., 1992). In the very shallow WTD areas,
278 the excess Es in GW results from the capillary rise of moisture from the shallow groundwater to the surface.

279

280 A significant factor in explaining how groundwater influences E is through changes in vertical drainage and recharge from the
281 aquifer to the soil column. Figure 2d shows that the vertical drainage (Dr) both increases and decreases depending on the location.
282 The addition of groundwater reduces vertical drainage by 74 mm yr⁻¹ where WTD is shallower than 5 m. In some regions, the
283 drainage increases with the inclusion of groundwater by up to 100 mm yr⁻¹, especially in the areas where WTD is ~ 5 m. This
284 is associated with the WTD being slightly below the bottom of the soil column (4.6 m). When the groundwater aquifer is nearly

285 full in GW, the wetter soil in the bottom layer leads to a much higher hydraulic conductivity in GW than in FD, leading to
286 higher vertical drainage in GW and a positive ΔDr . Inland, where the WTD tends to be much deeper there is no significant
287 difference in Dr between GW and FD.

288

289 Figure 2e shows the difference in recharge into the upper soil column (ΔQ_{rec}) between GW and FD. The recharge from the
290 aquifer into the bottom soil layer provides 17 mm yr^{-1} extra moisture in GW where has a WTD between $5\text{--}10 \text{ m}$ and 10 mm yr^{-1}
291 where the WTD is deeper than 10 m , helping to explain the changes in E and Et in areas with deep WTD. However, there is
292 no significant ΔQ_{rec} in regions with a shallow WTD ($\sim 5 \text{ mm yr}^{-1}$), suggesting the influence of groundwater is mainly via
293 reduced drainage in these locations. Recharge from the aquifer to the soil column can only occur when WTD is below the soil
294 column (bottom boundary at 4.6 m depth). If WTD is shallow and within the soil column, the interface is saturated and no
295 recharge from the aquifer to the soil column can occur and water only moves downwards by gravity.

296

297 The combined impact of reduced drainage in GW (Figure 2d) and recharge from the aquifer into the root-zone (Figure 2e) is an
298 increased water potential gradient between the drier top soil layers and the wetter deep soil layers, encouraging overnight
299 capillary rise. Taking the hot and dry January 2019 as an example, when the compound events occurred, Figure 2f shows the
300 maximum water stress factor difference ($\Delta\beta$) overnight (between 9 pm and 3 am, i.e. predawn when soil is relatively moist
301 following capillary lift overnight). We only consider rainless nights to exclude the impact of drainage induced by precipitation.
302 The water stress factor (β) is based on the root distribution and moisture availability in each soil layer and represents the soil
303 water stress on transpiration as water becomes limiting. Figure 2f implies that while the redistribution of moisture is small
304 overall, in some locations it can reduce moisture stress by up to 4–6%.

305 3.3 The impact of groundwater during heatwaves

306 We next explore whether the higher available moisture due to the inclusion of groundwater enables the canopy to cool itself via
307 evapotranspiration during heatwaves by examining the temperature difference between the simulated canopy temperature
308 (T_{canopy} , $^{\circ}\text{C}$) and the forced air temperature (T_{air} , $^{\circ}\text{C}$). We focus on the forested regions (Figure S2a) as the role of groundwater
309 in enhancing plant water availability was shown to be largest in these regions (Figure 2).

310

311 Figure 3a shows the average $T_{canopy} - T_{air}$ (ΔT , $^{\circ}\text{C}$) over the forested regions for summer heatwaves from the GW and FD
312 simulations, with the grey line indicating the median ΔT difference. During heatwaves, the inclusion of groundwater moistens
313 the soil and supports higher transpiration, cooling the canopy and reducing ΔT relative to FD by up to 0.76°C (e.g. summer
314 heatwaves in 2013). As the drought lengthens in time, the depletion of moisture gradually reduces this effect, from an average
315 reduction of 0.52°C of the first 3 years to 0.16°C of the last 3 years in Millennium Drought (Figure 3a). The impact of
316 groundwater is clear in the evaporative fraction (Figure 3b) where in periods of higher rainfall (e.g. 2010–2011; Figure S1), and
317 at the beginning of a drought (2001, 2017), the EF is higher (0.03 to 0.18). This implies more of the available energy is
318 exchanged with the atmosphere in the form of latent, rather than sensible heat. However, the strength of the cooling effect
319 decreases as the droughts extends and the transpiration difference (ΔEt , mm d^{-1}) diminishes quickly (Figure 3c) because the
320 vegetation becomes increasingly water-stressed (Figure 3d) which consequently limits transpiration. For all variables (ΔT , EF,
321 Et and β), the difference between GW and FD is greatest during the wetter periods (e.g., 2013) and in the first 1–2 years of the
322 multi-year drought (2001–2002 for the Millennium Drought or 2017–2018 for the recent drought). After the drought becomes
323 well established, the FD and GW simulations converge as depleting soil moisture reservoirs reduce the impact of groundwater
324 on canopy cooling and evaporative fluxes.

325

326 Figure 4a shows the spatial map of ΔT simulated in GW during heatwaves in the 2017–2019 drought. It indicates both land
327 cover type (Figure S2a) and WTD (Figure S5) contribute to the ΔT pattern. The evaporative cooling via transpiration is stronger
328 over the forested areas compared to cropland or grassland, and stronger in the regions with a wetter soil associated with a
329 shallower WTD. However, EF is mainly determined by WTD (compare Figure 4b and Figure S5). Inland, where the WTD is
330 deeper and the soil is drier, most of the net radiation absorbed by the land surface is partitioned into sensible rather than latent
331 heat (Figure 4b). However, in the coastal regions with a shallow WTD, the wetter soil reduces the water stress (Figure 4c),
332 enables a higher EF (Figure 4b), and alleviates heat stress on the leaves (Figure 4a). Along the coast where WTD is shallow,
333 GW simulates a cooler canopy temperature due to the higher evaporative cooling (Figure 4e) which is the consequence of a
334 lower soil water stress (Figure 4f) linked to the influence of groundwater (Figure S5).

335
336 Figure 5 shows the density scatter plot of ΔT versus WTD in S.E. Australia forested areas during heatwaves in 2000–2019. A
337 shallow WTD moderates the temperature difference between the canopy and the ambient air during heatwaves leading to a
338 smaller temperature difference. Meanwhile, as the WTD increases, due to the limited rooting depth in the model, the ability of
339 the groundwater to support transpiration and offset the impact of high air temperatures is reduced. Figure 5 shows a large amount
340 of variations, but nonetheless implies a threshold of ~ 6 m whereafter there is a decoupling and little influence from groundwater
341 during heatwaves. However, the absolute value of the threshold is likely CABLE-specific and associated with the assumption
342 of a 4.6 m soil depth, which also sets the maximum rooting depth (roots can only extend to the bottom of the soil and cannot
343 directly access the groundwater aquifer in CABLE). The CABLE soil depth comes from observational evidence of most roots
344 being situated within the top 4.6 m (Canadell et al. 1996). Since the model assumes no roots exist in the groundwater aquifer,
345 when the water table is below this depth, the water fluxes become largely uncoupled between the soil column and the
346 groundwater aquifer, leading to a negligible impact of GW below ~ 6 m depth.

347 3.4 The impact of groundwater during the drought and heatwave compound events

348 To examine the influence of groundwater on heatwaves occurring simultaneously with drought, we focus on a case study of the
349 record-breaking heatwaves in January 2019, which is the hottest month on record for the study region (Bureau of Meteorology,
350 2019). The unprecedented prolonged heatwave period started in early December 2018 and continued through January 2019 with
351 three peaks. We select two days (15th and 25th January 2019), when heatwaves spread across the study region, from the second
352 and third heatwave phases (Figure S6).

353
354 We evaluate CABLE T_{canopy} against MODIS LST observations, concentrating on forested areas where MODIS LST should
355 more closely reflect vegetation canopy temperatures, but note that this comparison is not direct as the satellite estimate will
356 contain contributions from the understorey and soil. Figures 6a-b show the good quality MODIS LST minus T_{air} at 2 pm
357 ($\Delta T_{\text{MOD_2pm}}$) over forested regions on the 15th and 25th January 2019, and Figures 6c-d display the matching GW-simulated ΔT
358 at 2 pm ($\Delta T_{\text{GW_2pm}}$). Overall, $\Delta T_{\text{GW_2pm}}$ increases from the coast to the interior in both heatwaves, consistent with the $\Delta T_{\text{MOD_2pm}}$
359 pattern in both heatwaves, albeit that $\Delta T_{\text{GW_2pm}}$ appears to be biased high relative to $\Delta T_{\text{MOD_2pm}}$ along the coastal forests (Figure
360 S7a-b).

361
362 Figure 6e-f shows the ΔT_{2pm} difference between GW and FD. Access to groundwater can reduce canopy temperature by up to
363 5°C, in particular where the WTD is shallow. While reductions of 5°C are clearly limited in spatial extent, the overall pattern of
364 cooling is quite widespread, and coincident with the groundwater-induced Et increase (Figure S8a-b), implying a reduction in
365 heat stress along coastal regions with a shallow WTD during heatwaves. Generally, GW matches MODIS LST better than FD
366 despite the bias in both simulations (compare Figure S7a-b and Figure S7c-d). Nevertheless, the temperature reduction between
367 GW and FD is still modest (< 1°C) for most of the forested regions. This may be related to the shallow root distribution assumed

368 in many LSMs, which prevents roots from directly accessing the moisture stored in the deeper soil (note, CABLE assumes 92%
369 of forest's roots are in the top 0.64 m, Figure S2b). To examine this possibility, we performed the deep root (DR) sensitivity
370 experiment which prescribed more roots in the deeper soil for forests (56% below 0.64 m depth). Figure 6g-h illustrates the
371 difference between ΔT_{2pm} in DR and ΔT_{GW_2pm} . By enabling access to moisture in the deeper soil, the LSM simulates further
372 cooling by 0.5–5°C across the forests associated with an E_t increase of 25–250 $W\ m^{-2}$ (Figure S8c-d). The prescribed deeper
373 roots also lead to an overall better simulation of ΔT at 2 pm relative to the MODIS LST (Figure S7e-f vs Figure S7a-b).

374
375 Figure 7 shows the diurnal cycles of ΔT for the two selected regions (red boxes in Figure 6) compared with the MODIS LST
376 estimates. The region highlighted for the 15th January (Figure 7a) has a WTD of 4–7 m, while the region highlighted for the 25th
377 January (Figure 7b) has a WTD < 4m (Figure S5). In both regions, the simulated ΔT is highest in FD, lower in GW and lowest
378 in DR. Where the WTD is 4–7m (Figure 7a), the three simulated ΔT are slightly lower than ΔT calculated by MODIS LST (red
379 squares). However, in the shallower WTD region (Figure 7b), the simulated ΔT between experiments is more dispersed across
380 experiments and exceeds the MODIS ΔT at both time points, implying that neglecting groundwater dynamics and deep roots is
381 more likely to cause an overestimation of heat stress in the shallower WTD region. The shallower WTD region (Figure 7b)
382 tends to have a high LAI coverage, implying that the MODIS LST represents a good approximation of the canopy temperature
383 over this region. Consequently, the lower MODIS ΔT implies that CABLE is likely underestimating transpiration, leading to an
384 overestimation of ΔT in all three simulations.

385 3.5 Constraints on groundwater mediation during the compound events

386 We finally probe the reasons for the apparent contradiction between the large impact of groundwater on E during drought
387 (Figure 2a) but a smaller impact on ΔT during the compound events (Figure 7). Figure 8 shows three factors (β , vapour pressure
388 deficit (D) and T_{air}) that constrain the impact of groundwater on ΔT in CABLE during heatwaves in January 2019. Figure 8a
389 shows the difference in ΔT between GW and FD as a function of $\Delta\beta$, suggesting that the inclusion of groundwater has a large
390 impact on ΔT when there is a coincidental and large difference in β between the GW and FD simulations. Figure 8b indicates a
391 clear threshold at $D = 3\ kPa$ where GW and FD converge, while Figure 8c shows a convergence threshold when the T_{air} exceeds
392 32°C. Above these two thresholds, access to groundwater seemingly becomes less important in mitigating plant heat stress.
393 There are two mechanisms in CABLE that explain this behaviour. First, as D increases, CABLE predicts that stomata begin to
394 close following a square root dependence (De Kauwe et al., 2015; Medlyn et al., 2011). Second, as T_{air} increases, photosynthesis
395 becomes inhibited as the temperature exceeds the optimum for photosynthesis. In both instances, evaporative cooling is reduced,
396 regardless of the root zone moisture state dictated by groundwater access. That is to say, access to groundwater has limited
397 capacity to directly mediate the heat stress on plants during a compound event when the air is very dry, or very hot.

398 4 Discussion

399 In the absence of direct measurements, we used the CABLE-GW LSM, constrained by satellite observations to investigate how
400 groundwater influences ecosystems under conditions of co-occurring droughts and heatwaves. We found that the influence of
401 groundwater was most important during the wetter periods and the first ~ two years of a multi-year drought (~2001–2002 and
402 2017–2018; Figure 1 and 3). This primarily occurred via impeding gravity-driven drainage (Figure 2d) but also via capillary
403 rise from the groundwater aquifer (Figure 2e). This moistening enabled the vegetation to sustain higher E for at least a year
404 (Figure S9). As the droughts progressed into multi-year events, the impact of groundwater diminished due to a depletion of soil
405 moisture stores regardless of whether groundwater dynamics were simulated.

407 When a heatwave occurs during a drought, and in particular early in a drought, the extra transpiration enabled by representing
408 groundwater dynamics helps reduce the heat stress on vegetation (e.g. the reduction of 0.64°C of ΔT over the forests in 2002,
409 Figure 3a). This effect is particularly pronounced in regions with a shallower WTD (e.g. where the groundwater was within the
410 first 5 m, there was a 0.5°C mean reduction in ΔT in the recent drought, Figure 4d). Importantly, the role played by groundwater
411 diminishes as the drought lengthens beyond two years (Figure 3). Additionally, either the lack of deep roots or stomatal closure
412 caused by high D/T_{air} can reduce the additional transpiration induced by groundwater. The latter plant physiology feedback
413 dominates during heatwaves co-occurring with drought, even if the groundwater's influence has increased root-zone water
414 availability.

415

416 Our results highlight the impact of groundwater on both land surface states (e.g. soil moisture) and on surface fluxes and how
417 this impact varies with the length and intensity of droughts and heatwaves. The results imply that the dominant mechanism by
418 which groundwater buffered transpiration was through impeding gravity-driven drainage. We found a limited role for upward
419 water movement from aquifer due to simulated shallow WTD (which was broadly consistent with the observations in Fan et al.,
420 2013). Further work will be necessary to understand how groundwater interacts with droughts and heatwaves and what these
421 interactions mean for terrestrial ecosystems and the occurrence of the compound extreme events, particularly under the
422 projection of intensifying droughts (Ukkola et al., 2020) and heatwaves (Cowan et al., 2014).

423 **4.1 Changes in the role of groundwater in multi-year droughts**

424 Groundwater is the slowest part of the terrestrial water cycle to change (Condon et al., 2020) and can have a memory of multi-
425 year variations in rainfall (Martínez-de la Torre and Miguez-Macho, 2019; Martinez et al., 2016a). Our results show that the
426 effect of groundwater on the partitioning of available energy between latent and sensible heat fluxes is influenced by the length
427 of drought. As the drought extends in time, the extra E sustained by groundwater decreases (e.g. during the Millennium drought,
428 Figure S9). The role of a drying landscape in modifying the partitioning of available energy between latent and sensible heat
429 fluxes is well known and has been extensively studied (Fan, 2015; Miralles et al., 2019; Seneviratne et al., 2010). Our results
430 add to the knowledge by quantifying the extent of the groundwater control, and eliciting the timescales of influence and the
431 mechanisms at play. The importance of vegetation-groundwater interactions on multi-year timescales has been identified
432 previously. Humphrey et al. (2018) hypothesised that climate models may underestimate the amplitude of global net ecosystem
433 exchange because of a lack of deep-water access. Our regional based results support this hypothesis and in particular highlight
434 the importance of groundwater for explaining the amplitude of fluxes in wet periods, as well as sustaining evapotranspiration
435 during drought (Figure 1).

436 **4.2 Implications for land-atmosphere feedbacks during compound events**

437 Our results show that during drought-heatwave compound events, the existence of groundwater eases the heat stress on the
438 forest canopy and reduces the sensible heat flux to atmosphere. This has the potential to reduce heat accumulating in the
439 boundary layer and help ameliorate the intensity of a heatwave (Keune et al., 2016; Zipper et al., 2019). The presence of
440 groundwater helps dampen a positive feedback loop whereby during drought-heatwave compound events, the high exchange of
441 sensible and low exchange of latent heat can heat the atmosphere and increase the atmospheric demand for water (De Boeck et
442 al., 2010; Massmann et al., 2019), intensifying drying (Miralles et al., 2014). The lack of groundwater in many LSMs suggests
443 a lack of this moderating process and consequently a risk of overestimating the positive feedback on the boundary layer in
444 coupled climate simulations. Our results show that neglecting groundwater leads to an average overestimate in canopy
445 temperature by 0.2–1°C where the WTD is shallow (Figure 4d), but as much as 5°C in single heatwave events (Figure 6e-f),
446 leading to an increase in the sensible heat flux (Figure 4e).

447

448 The capacity of groundwater to moderate this positive land-atmosphere feedback is via modifying soil water availability. Firstly,
449 soil water availability influenced by WTD affects how much water is available for E. In the shallow WTD regions, the higher
450 soil water is likely to suppress the mutual enhancement of droughts and heatwaves (Keune et al., 2016; Zipper et al., 2019),
451 particularly early in a drought. However, this suppression becomes weaker as the WTD deepens, in particular at depths beneath
452 the root zone (e.g. 4.6 m in CABLE-GW) or as a drought lengthens. Our results imply the land-amplification of heatwaves is
453 likely stronger in the inland regions (Hirsch et al., 2019) where the WTD is lower than 5 m and the influence of groundwater
454 diminishes (Figure S5), and once a drought has intensified significantly.

455

456 On a dry and hot heatwave afternoon, plant physiology feedbacks to high D and high T_{air} dominate transpiration and reduce the
457 influence of groundwater in moderating heatwaves. In CABLE, stomatal closure occurs either directly due to high D (>3 kPa)
458 (De Kauwe et al. 2015) or indirectly due to biochemical feedbacks on photosynthesis at high T_{air} ($>32^{\circ}\text{C}$) (Kowalczyk et al.,
459 2006); both processes reduce transpiration to near zero, eliminating the buffering effect of groundwater on canopy temperatures.
460 While the timing of the onset of these physiology feedbacks varies across LSMs due to different parameterised sensitivities of
461 stomatal conductance to atmospheric demand (Ball et al., 1987; Leuning et al., 1995) and different temperature dependence
462 parameterisations (Badger and Collatz, 1977; Bernacchi et al., 2001; Crous et al., 2013), importantly, stomatal closure during
463 heat extremes would be model invariant.

464 4.3 Uncertainties and future directions

465 Our study uses a single LSM and consequently the parameterisations included in CABLE-GW influence the quantification of
466 the role of groundwater on droughts and heatwaves. We note CABLE-GW has been extensively evaluated for water cycle
467 processes (Decker, 2015; Decker et al., 2017; Mu et al., 2021; Ukkola et al., 2016b), but evaluation for groundwater interactions
468 remains limited due to the lack of suitable observations (e.g. regional WTD monitoring or detailed knowledge of the distribution
469 of root depths). Figure 1 gives us confidence that CABLE-GW is performing well, based on the evaluation against the GRACE,
470 DOLCE and GLEAM products, as well as previous work that showed the capacity of CABLE-GW to simulate E well (Decker,
471 2015; Decker et al., 2017). However, we also note that key model parameterisations that may influence the role of groundwater
472 are particularly uncertain.

473

474 We need to be cautious about the “small” groundwater impact on the canopy temperature and associated turbulent energy fluxes
475 during high D or high T_{air} (Figure 3, 4, 6 and 7). The thresholds of D and T_{air} currently assumed by LSMs are in fact likely to
476 be species specific. Australian trees in particular have evolved a series of physiological adaptations to reduce the negative
477 impact of heat extremes. It is important to note that most LSMs parameterise their stomatal response to D for moderate ranges
478 (< 2 kPa), which leads to significant biases at high D (Yang et al., 2019), a feature common in Australia and during heatwaves
479 in general. New theory is needed to ensure that models adequately capture the full range of stomatal response to variability in
480 D (low and high ranges). Similarly, while there is strong evidence to suggest that the optimum temperature for photosynthesis
481 does not vary predictably with the climate of species origin (Kumarathunge et al., 2019) (implying model parameterisations do
482 not need to vary with species), findings from studies do vary (Cunningham and Reed 2002; Reich et al. 2015). Moreover,
483 evidence that plants acclimate their photosynthetic temperature response is strong (Kattge and Knorr, 2007; Kumarathunge et
484 al., 2019; Mercado et al., 2018; Smith et al., 2016; Smith and Dukes, 2013). As a result, it is likely that LSMs currently
485 underestimate groundwater influence during heatwaves due to the interaction with plant physiology feedbacks. This is a key
486 area requiring further investigation. For example, Drake et al. (2018) demonstrated that during a 4-day heatwave $> 43^{\circ}\text{C}$,
487 Australian *Eucalyptus parramattensis* trees did not reduce transpiration to zero as models would commonly predict, allowing
488 the trees to persist unharmed in a whole-tree chamber experiment. Although De Kauwe et al. (2019) did not find strong support
489 for this phenomenon across eddy covariance sites, if this physiological response is common across Australian woodlands, it

would change our view on the importance of soil water availability (therefore groundwater) on the evolution of heatwave or even compound events. Coupled model sensitivity experiments may be important to determine the magnitude that such a physiological feedback would present and could guide the direction of future field/manipulation experiments.

Root distribution and root function and thereby how roots utilise groundwater are uncertain in models (Arora and Boer, 2003; Drewniak, 2019; Wang et al., 2018; Warren et al., 2015) and indeed in observations (Fan et al., 2017; Jackson et al., 1996; Schenk and Jackson, 2002). Models often ignore how roots forage for water and respond to moisture heterogeneity, limiting the model's ability to accurately reflect the plant usage of groundwater (Warren et al., 2015). In LSMs, roots are typically parameterised using a fixed distribution and normally ignore water uptake from deep roots. This assumption neglects any climatological impact of root distribution and the differentiation in root morphology and function (fine roots vs tap roots), leading to a potential underestimation of groundwater utilization in LSMs (see our deep root experiment, Figure 6g-h). This assumption may be particularly problematic in Australia where vegetation has developed significant adaptation strategies to cope with both extreme heat and drought, including deeply rooted vegetation that can access groundwater (Bartle et al., 1980; Dawson and Pate, 1996; Eamus et al., 2015; Eberbach and Burrows, 2006; Fan et al., 2017). We also note that CABLE does not directly consider hydraulic redistribution, defined as the passive water movement via plant roots from moister to drier soil layers (Burgess et al., 1998; Richards and Caldwell, 1987). Neglecting hydraulic redistribution has the potential to underestimate the groundwater transported upwards and understate the importance of groundwater on ecosystems.

On the atmosphere side, the existence of groundwater increases the water flux from the land to atmosphere, particularly in regions of shallow WTD, during the first 1–2 years of a drought. This has the potential to moisten the lower atmosphere and may encourage precipitation (Anyah et al., 2008; Jiang et al., 2009; Martinez et al., 2016b; Maxwell et al., 2011). However, our experiments are uncoupled from the atmosphere so while there is the potential for the higher E to affect the boundary layer moisture (Bonetti et al., 2015; Gilbert et al., 2017; Maxwell et al., 2007), clouds and precipitation, we cannot conclude that it would until we undertake future coupled simulations.

Finally, we note we have focused on the role of groundwater in a natural environment. Humans extract large quantities of groundwater in many regions (Döll et al., 2014; Wada, 2016). Adding human management of groundwater into LSMs enables an examination of how this affects the vulnerability of ecosystems to heatwaves and drought, and may ultimately identify those vulnerable ecosystems close to tipping points that are priorities for protection.

5 Conclusions

In conclusion, we used the CABLE LSM, constrained by satellite observations, to explore the timescales and extent to which groundwater influences vegetation function and turbulent energy fluxes during multi-year droughts. We showed that groundwater moistened the soil during the first ~two years of a multi-year drought which enabled the vegetation to sustain higher evaporation (50–200 mm yr⁻¹ over the coastal forest regions) during drought onset. This cooled the forest canopy on average by 0.03–0.76°C in heatwaves during 2001–2019 and as much as 5°C in regions of shallow water table depths in the heatwave in January 2019, helping to moderate the heat stress on vegetation during heatwaves. However, the ability of groundwater to buffer vegetation function varied with the length and intensity of droughts and heatwaves, with its influence decreasing with prolonged drought conditions. Importantly, we also demonstrated that the capacity of the groundwater to buffer evaporative fluxes during heatwaves is constrained by plant physiology feedbacks which regulate stomatal control, irrespective of soil water status. Given increased risk of regional heatwaves and droughts in the future, the role of groundwater on land-atmosphere feedbacks and on terrestrial ecosystems needs to be better understood in order to constrain future projections.

531 **Code and data availability**

532 The CABLE code is available at <https://trac.nci.org.au/trac/cable> (last access: 4 August 2021) (NCI, 2021) after registration.
533 Here, we use CABLE revision r7765. Scripts for plotting and processing model outputs are available at
534 <https://doi.org/10.5281/zenodo.5158498> (Mu, 2021). DOLCE version 2 dataset is available from the NCI data catalogue at
535 <http://dx.doi.org/10.25914/5f1664837ef06> (Hobeichi, 2020). GRACE land is available at <http://grace.jpl.nasa.gov>, supported
536 by the NASA MEaSUREs Program. GLEAM dataset is available at <https://www.gleam.eu/>. MOD11A1 MODIS/Terra Land
537 Surface Temperature and the Emissivity Daily L3 Global 1km and MYD11A1 MODIS/Aqua Land Surface Temperature and
538 the Emissivity Daily L3 Global 1km datasets were acquired from the NASA Land Processed Distributed Active Archive Center
539 (LP DAAC), located in the USGS Earth Resources Observation and Science (EROS) Center in Sioux Falls, South Dakota, USA
540 (<https://lpdaacsvc.cr.usgs.gov/appeears/>).
541

541

542 **Author contributions**

543 MM, MGDK, AJP and AMU conceived the study, designed the model experiments, investigated the simulations and drafted
544 the manuscript. SH and PRB provided the evaluation and the meteorology forcing datasets. All authors participated in the
545 discussion and revision of the manuscript.
546

547 **Acknowledgements**

548 Mengyuan Mu, Martin G. De Kauwe, Andy J. Pitman, Anna M. Ukkola and Sanaa Hobeichi acknowledge support from the
549 Australian Research Council (ARC) Centre of Excellence for Climate Extremes (CE170100023). Mengyuan Mu acknowledges
550 support from the UNSW University International Postgraduate Award (UIPA) scheme. Martin G. De Kauwe and Andy J. Pitman
551 acknowledge support from the ARC Discovery Grant (DP190101823) and Anna M. Ukkola support from the ARC Discovery
552 Early Career Researcher Award (DE200100086). Martin G. De Kauwe acknowledges support from the NSW Research
553 Attraction and Acceleration Program (RAAP). We thank the National Computational Infrastructure at the Australian National
554 University, an initiative of the Australian Government, for access to supercomputer resources. Mengyuan Mu thanks the
555 University of Nanjing for hosting her research through 2020.
556

557 **References**

558 Abramowitz, G., Leuning, R., Clark, M. and Pitman, A.: Evaluating the performance of land surface models, *J. Clim.*, 21(21),
559 5468–5481, doi:10.1175/2008JCLI2378.1, 2008.

560 Allen, C. D., Macalady, A. K., Chenchouni, H., Bachelet, D., McDowell, N., Vennetier, M., Kitzberger, T., Rigling, A.,
561 Breshears, D. D., Hogg, E. H. (Ted), Gonzalez, P., Fensham, R., Zhang, Z., Castro, J., Demidova, N., Lim, J.-H., Allard,
562 G., Running, S. W., Semerci, A. and Cobb, N.: A global overview of drought and heat-induced tree mortality reveals
563 emerging climate change risks for forests, *For. Ecol. Manage.*, 259(4), 660–684, doi:10.1016/j.foreco.2009.09.001, 2010.

564 Allen, C. D., Breshears, D. D. and McDowell, N. G.: On underestimation of global vulnerability to tree mortality and forest die-
565 off from hotter drought in the Anthropocene, *Ecosphere*, 6(8), art129, doi:10.1890/ES15-00203.1, 2015.

566 Anyah, R. O., Weaver, C. P., Miguez-Macho, G., Fan, Y. and Robock, A.: Incorporating water table dynamics in climate
567 modeling: 3. Simulated groundwater influence on coupled land-atmosphere variability, *J. Geophys. Res.*, 113(D7), D07103,
568 doi:10.1029/2007JD009087, 2008.

569 Arora, V. K. and Boer, G. J.: A representation of variable root distribution in dynamic vegetation models, *Earth Interact.*, 7(6),
570 1–19, doi:10.1175/1087-3562(2003)007<0001:AROVRD>2.0.CO;2, 2003.

571 Badger, M. R. and Collatz, G. J.: Studies on the kinetic mechanism of RuBP carboxylase and oxygenase reactions, with
572 particular reference to the effect of temperature on kinetic parameters, *Year book–Carnegie Institution of Washington*,
573 Baltimore, Maryland, USA, 355–361 pp., 1977.

574 Ball, J. T., Woodrow, I. E. and Berry, J. A.: A model predicting stomatal conductance and its contribution to the control of
575 photosynthesis under different environmental conditions, in *Progress in Photosynthesis Research*, Springer Netherlands,
576 Dordrecht, Netherlands, 221–224 pp., doi:10.1007/978-94-017-0519-6_48, 1987.

577 Bartle, G. A., Murray, A. M. and Macpherson, D. K.: The distribution of root length, and the limits to flow of soil water to roots
578 in a dry sclerophyll forest, *For. Sci.*, 26(4), 656–664, doi:10.1093/forestscience/26.4.656, 1980.

579 Bernacchi, C. J., Singsaas, E. L., Pimentel, C., Portis Jr, A. R. and Long, S. P.: Improved temperature response functions for
580 models of Rubisco-limited photosynthesis, *Plant. Cell Environ.*, 24(2), 253–259, doi:10.1111/j.1365-3040.2001.00668.x,
581 2001.

582 Birami, B., Gattmann, M., Heyer, A. G., Grote, R., Arneth, A. and Ruehr, N. K.: Heat waves alter carbon allocation and increase
583 mortality of Aleppo Pine under dry conditions, *Front. For. Glob. Chang.*, 1, doi:10.3389/ffgc.2018.00008, 2018.

584 De Boeck, H. J., Dreesen, F. E., Janssens, I. A. and Nijs, I.: Climatic characteristics of heat waves and their simulation in plant
585 experiments, *Glob. Chang. Biol.*, 16(7), 1992–2000, doi:10.1111/j.1365-2486.2009.02049.x, 2010.

586 Bonetti, S., Manoli, G., Domec, J. C., Putti, M., Marani, M. and Katul, G. G.: The influence of water table depth and the free
587 atmospheric state on convective rainfall predisposition, *Water Resour. Res.*, 51(4), 2283–2297,
588 doi:10.1002/2014WR016431, 2015.

589 Bureau of Meteorology: Special Climate Statement 43-extreme heat in January 2013. [online] Available from:
590 <http://www.bom.gov.au/climate/current/statements/scs43e.pdf>, 2013.

591 Bureau of Meteorology: Special Climate Statement 61-exceptional heat in southeast Australia in early 2017. [online] Available
592 from: <http://www.bom.gov.au/climate/current/statements/scs61.pdf>, 2017.

593 Bureau of Meteorology: Special Climate Statement 68—widespread heatwaves during December 2018 and January 2019.
594 [online] Available from: <http://www.bom.gov.au/climate/current/statements/scs68.pdf> (Accessed 18 May 2020), 2019.

595 Burgess, S. S. O., Adams, M. A., Turner, N. C. and Ong, C. K.: The redistribution of soil water by tree root systems, *Oecologia*,
596 115(3), 306–311, doi:10.1007/s004420050521, 1998.

597 Canadell, J., Jackson, R. B., Ehleringer, J. B., Mooney, H. A., Sala, O. E. and Schulze, E.-D.: Maximum rooting depth of
598 vegetation types at the global scale, *Oecologia*, 108(4), 583–595, doi:10.1007/BF00329030, 1996.

599 Ciais, P., Reichstein, M., Viovy, N., Granier, A., Ogée, J., Allard, V., Aubinet, M., Buchmann, N., Bernhofer, C., Carrara, A.,
600 Chevallier, F., De Noblet, N., Friend, A. D., Friedlingstein, P., Grünwald, T., Heinesch, B., Keronen, P., Knohl, A., Krinner,
601 G., Loustau, D., Manca, G., Matteucci, G., Miglietta, F., Ourcival, J. M., Papale, D., Pilegaard, K., Rambal, S., Seufert, G.,

602 Soussana, J. F., Sanz, M. J., Schulze, E. D., Vesala, T. and Valentini, R.: Europe-wide reduction in primary productivity
603 caused by the heat and drought in 2003, *Nature*, 437(7058), 529–533, doi:10.1038/nature03972, 2005.

604 Condon, L. E., Atchley, A. L. and Maxwell, R. M.: Evapotranspiration depletes groundwater under warming over the contiguous
605 United States, *Nat. Commun.*, 11(1), 873, doi:10.1038/s41467-020-14688-0, 2020.

606 Cowan, T., Purich, A., Perkins, S., Pezza, A., Boschat, G. and Sadler, K.: More frequent, longer, and hotter heat waves for
607 Australia in the twenty-first century, *J. Clim.*, 27(15), 5851–5871, doi:10.1175/JCLI-D-14-00092.1, 2014.

608 Crous, K. Y., Quentin, A. G., Lin, Y.-S., Medlyn, B. E., Williams, D. G., Barton, C. V. M. and Ellsworth, D. S.: Photosynthesis
609 of temperate *Eucalyptus globulus* trees outside their native range has limited adjustment to elevated CO₂ and climate
610 warming, *Glob. Chang. Biol.*, 19(12), 3790–3807, doi:10.1111/gcb.12314, 2013.

611 D'Odorico, P. and Porporato, A.: Preferential states in soil moisture and climate dynamics, *Proc. Natl. Acad. Sci.*, 101(24),
612 8848–8851, doi:10.1073/pnas.0401428101, 2004.

613 Dawson, T. E. and Pate, J. S.: Seasonal water uptake and movement in root systems of Australian phreatophytic plants of
614 dimorphic root morphology: a stable isotope investigation, *Oecologia*, 107(1), 13–20, doi:10.1007/BF00582230, 1996.

615 Decker, M.: Development and evaluation of a new soil moisture and runoff parameterization for the CABLE LSM including
616 subgrid-scale processes, *J. Adv. Model. Earth Syst.*, 7(4), 1788–1809, doi:10.1002/2015MS000507, 2015.

617 Decker, M., Or, D., Pitman, A. and Ukkola, A.: New turbulent resistance parameterization for soil evaporation based on a pore-
618 scale model: Impact on surface fluxes in CABLE, *J. Adv. Model. Earth Syst.*, 9(1), 220–238, doi:10.1002/2016MS000832,
619 2017.

620 van Dijk, A. I. J. M. J. M., Beck, H. E., Crosbie, R. S., de Jeu, R. A. M., Liu, Y. Y., Podger, G. M., Timbal, B. and Viney, N.
621 R.: The Millennium Drought in southeast Australia (2001–2009): Natural and human causes and implications for water
622 resources, ecosystems, economy, and society, *Water Resour. Res.*, 49(2), 1040–1057, doi:10.1002/wrcr.20123, 2013.

623 Döll, P., Müller Schmied, H., Schuh, C., Portmann, F. T. and Eicker, A.: Global-scale assessment of groundwater depletion and
624 related groundwater abstractions: Combining hydrological modeling with information from well observations and GRACE
625 satellites, *Water Resour. Res.*, 50(7), 5698–5720, doi:10.1002/2014WR015595, 2014.

626 Drake, J. E., Tjoelker, M. G., Vårhammar, A., Medlyn, B. E., Reich, P. B., Leigh, A., Pfautsch, S., Blackman, C. J., López, R.,
627 Aspinwall, M. J., Crous, K. Y., Duursma, R. A., Kumarathunge, D., De Kauwe, M. G., Jiang, M., Nicotra, A. B., Tissue,
628 D. T., Choat, B., Atkin, O. K. and Barton, C. V. M. M.: Trees tolerate an extreme heatwave via sustained transpirational
629 cooling and increased leaf thermal tolerance, *Glob. Chang. Biol.*, 24(6), 2390–2402, doi:10.1111/gcb.14037, 2018.

630 Drewniak, B. A.: Simulating dynamic roots in the energy exascale earth system land model, *J. Adv. Model. Earth Syst.*, 11(1),
631 338–359, doi:10.1029/2018MS001334, 2019.

632 Eamus, D. and Froend, R.: Groundwater-dependent ecosystems: the where, what and why of GDEs, *Aust. J. Bot.*, 54(2), 91,
633 doi:10.1071/BT06029, 2006.

634 Eamus, D., Zolfaghari, S., Villalobos-Vega, R., Cleverly, J. and Huete, A.: Groundwater-dependent ecosystems: recent insights
635 from satellite and field-based studies, *Hydrol. Earth Syst. Sci.*, 19(10), 4229–4256, doi:10.5194/hess-19-4229-2015, 2015.

636 Eberbach, P. L. and Burrows, G. E.: The transpiration response by four topographically distributed Eucalyptus species, to
637 rainfall occurring during drought in south eastern Australia, *Physiol. Plant.*, 127(3), 483–493, doi:10.1111/j.1399-
638 3054.2006.00762.x, 2006.

639 Fan, Y.: Groundwater in the Earth's critical zone: Relevance to large-scale patterns and processes, *Water Resour. Res.*, 51(5),
640 3052–3069, doi:10.1002/2015WR017037, 2015.

641 Fan, Y., Li, H. and Miguez-Macho, G.: Global patterns of groundwater table depth, *Science*, 339(6122), 940–943,
642 doi:10.1126/science.1229881, 2013.

643 Fan, Y., Miguez-Macho, G., Jobbágy, E. G., Jackson, R. B. and Otero-Casal, C.: Hydrologic regulation of plant rooting depth,
644 *Proc. Natl. Acad. Sci.*, 114(40), 10572–10577, doi:10.1073/pnas.1712381114, 2017.

645 Fischer, E. M., Seneviratne, S. I., Vidale, P. L., Lüthi, D. and Schär, C.: Soil moisture–atmosphere interactions during the 2003
646 European summer heat wave, *J. Clim.*, 20(20), 5081–5099, doi:10.1175/JCLI4288.1, 2007.

647 Gale, M. R. and Grigal, D. F.: Vertical root distributions of northern tree species in relation to successional status, *Can. J. For.
648 Res.*, 17(8), 829–834, doi:10.1139/x87-131, 1987.

649 Geange, S. R., Arnold, P. A., Catling, A. A., Coast, O., Cook, A. M., Gowland, K. M., Leigh, A., Notarnicola, R. F., Posch, B.
650 C., Venn, S. E., Zhu, L. and Nicotra, A. B.: The thermal tolerance of photosynthetic tissues: a global systematic review
651 and agenda for future research, *New Phytol.*, 229(5), 2497–2513, doi:10.1111/nph.17052, 2021.

652 Gilbert, J. M., Maxwell, R. M. and Gochis, D. J.: Effects of water-table configuration on the planetary boundary layer over the
653 San Joaquin River Watershed, California, *J. Hydrometeorol.*, 18(5), 1471–1488, doi:10.1175/JHM-D-16-0134.1, 2017.

654 Griffith, S. J., Bale, C. and Adam, P.: Environmental correlates of coastal heathland and allied vegetation, *Aust. J. Bot.*, 56(6),
655 512, doi:10.1071/BT06147, 2008.

656 Haverd, V., Raupach, M. R., Briggs, P. R., Canadell, J. G., Isaac, P., Pickett-Heaps, C., Roxburgh, S. H., van Gorsel, E., Viscarra
657 Rossel, R. A. and Wang, Z.: Multiple observation types reduce uncertainty in Australia's terrestrial carbon and water cycles,
658 *Biogeosciences*, 10(3), 2011–2040, doi:10.5194/bg-10-2011-2013, 2013.

659 Hengl, T., Mendes de Jesus, J., Heuvelink, G. B. M., Ruperez Gonzalez, M., Kilibarda, M., Blagotić, A., Shangguan, W.,
660 Wright, M. N., Geng, X., Bauer-Marschallinger, B., Guevara, M. A., Vargas, R., MacMillan, R. A., Batjes, N. H., Leenaars,
661 J. G. B., Ribeiro, E., Wheeler, I., Mantel, S. and Kempen, B.: SoilGrids250m: Global gridded soil information based on
662 machine learning, edited by B. Bond-Lamberty, *PLoS One*, 12(2), e0169748, doi:10.1371/journal.pone.0169748, 2017.

663 Hirsch, A. L., Evans, J. P., Di Virgilio, G., Perkins-Kirkpatrick, S. E., Argüeso, D., Pitman, A. J., Carouge, C. C., Kala, J.,
664 Andrys, J., Petrelli, P. and Rockel, B.: Amplification of Australian heatwaves via local land-atmosphere coupling, *J. Geophys. Res. Atmos.*, 124(24), 13625–13647, doi:10.1029/2019JD030665, 2019.

666 Hobeichi, S.: Derived Optimal Linear Combination Evapotranspiration - DOLCE v2.1, doi:10.25914/5f1664837ef06, 2020.

667 Hobeichi, S., Abramowitz, G. and Evans, J. P.: Robust historical evapotranspiration trends across climate regimes, *Hydrol.
668 Earth Syst. Sci.*, 25(7), 3855–3874, doi:10.5194/hess-25-3855-2021, 2021.

669 Horton, R. M., Mankin, J. S., Lesk, C., Coffel, E. and Raymond, C.: A review of recent advances in research on extreme heat
670 events, *Curr. Clim. Chang. Reports*, 2(4), 242–259, doi:10.1007/s40641-016-0042-x, 2016.

671 Humphrey, V., Zscheischler, J., Ciais, P., Gudmundsson, L., Sitch, S. and Seneviratne, S. I.: Sensitivity of atmospheric CO₂
672 growth rate to observed changes in terrestrial water storage, *Nature*, 560(7720), 628–631, doi:10.1038/s41586-018-0424-
673 4, 2018.

674 Ibáñez, I., Acharya, K., Juno, E., Karounos, C., Lee, B. R., McCollum, C., Schaffer-Morrison, S. and Tourville, J.: Forest
675 resilience under global environmental change: Do we have the information we need? A systematic review, edited by R.
676 Zang, *PLoS One*, 14(9), e0222207, doi:10.1371/journal.pone.0222207, 2019.

677 Jackson, R. B., Canadell, J., Ehleringer, J. R., Mooney, H. A., Sala, O. E. and Schulze, E. D.: A global analysis of root
678 distributions for terrestrial biomes, *Oecologia*, 108(3), 389–411, doi:10.1007/BF00333714, 1996.

679 Jiang, X., Niu, G.-Y. and Yang, Z.-L.: Impacts of vegetation and groundwater dynamics on warm season precipitation over the
680 Central United States, *J. Geophys. Res.*, 114(D6), D06109, doi:10.1029/2008JD010756, 2009.

681 Jones, D., Wang, W. and Fawcett, R.: High-quality spatial climate data-sets for Australia, *Aust. Meteorol. Oceanogr. J.*, 58(04),
682 233–248, doi:10.22499/2.5804.003, 2009.

683 Jyoteeshkumar reddy, P., Sharples, J. J., Lewis, S. C. and Perkins-Kirkpatrick, S. E.: Modulating influence of drought on the
684 synergy between heatwaves and dead fine fuel moisture content of bushfire fuels in the Southeast Australian region,
685 *Weather Clim. Extrem.*, 31, 100300, doi:10.1016/j.wace.2020.100300, 2021.

686 Kattge, J. and Knorr, W.: Temperature acclimation in a biochemical model of photosynthesis: a reanalysis of data from 36
687 species, *Plant. Cell Environ.*, 30(9), 1176–1190, doi:10.1111/j.1365-3040.2007.01690.x, 2007.

688 De Kauwe, M. G., Kala, J., Lin, Y. S., Pitman, A. J., Medlyn, B. E., Duursma, R. A., Abramowitz, G., Wang, Y. P. and Miralles,
689 D. G.: A test of an optimal stomatal conductance scheme within the CABLE land surface model, *Geosci. Model Dev.*, 8(2),
690 431–452, doi:10.5194/gmd-8-431-2015, 2015.

691 De Kauwe, M. G., Medlyn, B. E., Pitman, A. J., Drake, J. E., Ukkola, A., Griebel, A., Pendall, E., Prober, S. and Roderick, M.:
692 Examining the evidence for decoupling between photosynthesis and transpiration during heat extremes, *Biogeosciences*,
693 16(4), 903–916, doi:10.5194/bg-16-903-2019, 2019.

694 De Kauwe, M. G., Medlyn, B. E., Ukkola, A. M., Mu, M., Sabot, M. E. B. B., Pitman, A. J., Meir, P., Cernusak, L. A., Rifai, S.
695 W., Choat, B., Tissue, D. T., Blackman, C. J., Li, X., Roderick, M. and Briggs, P. R.: Identifying areas at risk of drought-
696 induced tree mortality across South-Eastern Australia, *Glob. Chang. Biol.*, 26(10), 5716–5733, doi:10.1111/gcb.15215,
697 2020.

698 Keune, J., Gasper, F., Goergen, K., Hense, A., Shrestha, P., Sulis, M. and Kollet, S.: Studying the influence of groundwater
699 representations on land surface-atmosphere feedbacks during the European heat wave in 2003, *J. Geophys. Res. Atmos.*,
700 121(22), 13,301–13,325, doi:10.1002/2016JD025426, 2016.

701 Kim, W., Iizumi, T. and Nishimori, M.: Global Patterns of Crop Production Losses Associated with Droughts from 1983 to
702 2009, *J. Appl. Meteorol. Climatol.*, 58(6), 1233–1244, doi:10.1175/JAMC-D-18-0174.1, 2019.

703 Kowalczyk, E. A., Wang, Y. P. and Law, R. M.: The CSIRO Atmosphere Biosphere Land Exchange (CABLE) model for use
704 in climate models and as an offline model, *CSIRO Mar. Atmos. Res. Pap.*, 13(November 2015), 1–42,
705 doi:10.4225/08/58615c6a9a51d, 2006.

706 Kuginis, L., Dabovic, J., Burne, G., Raine, A. and Hemakumara, H.: Methods for the identification of high probability
707 groundwater dependent vegetation ecosystems, DPI Water: Sydney, NSW. [online] Available from: www.dpi.nsw.gov.au,
708 2016.

709 Kumarathunge, D. P., Medlyn, B. E., Drake, J. E., Tjoelker, M. G., Aspinwall, M. J., Battaglia, M., Cano, F. J., Carter, K. R.,
710 Cavalieri, M. A., Cernusak, L. A., Chambers, J. Q., Crous, K. Y., De Kauwe, M. G., Dillaway, D. N., Dreyer, E., Ellsworth,
711 D. S., Ghannoum, O., Han, Q., Hikosaka, K., Jensen, A. M., Kelly, J. W. G. G., Kruger, E. L., Mercado, L. M., Onoda, Y.,
712 Reich, P. B., Rogers, A., Slot, M., Smith, N. G., Tarvainen, L., Tissue, D. T., Togashi, H. F., Tribuzy, E. S., Uddling, J.,
713 Vårhammar, A., Wallin, G., Warren, J. M. and Way, D. A.: Acclimation and adaptation components of the temperature
714 dependence of plant photosynthesis at the global scale, *New Phytol.*, 222(2), 768–784, doi:10.1111/nph.15668, 2019.

715 Landerer, F. W., Flechtner, F. M., Save, H., Webb, F. H., Bandikova, T., Bertiger, W. I., Bettadpur, S. V., Byun, S. H., Dahle,
716 C., Dobslaw, H., Fahnestock, E., Harvey, N., Kang, Z., Kruizinga, G. L. H., Loomis, B. D., McCullough, C., Murböck,
717 M., Nagel, P., Paik, M., Pie, N., Poole, S., Strekalov, D., Tamisiea, M. E., Wang, F., Watkins, M. M., Wen, H., Wiese, D.
718 N. and Yuan, D.: Extending the global mass change data record: GRACE Follow-On instrument and science data
719 performance, *Geophys. Res. Lett.*, 47(12), doi:10.1029/2020GL088306, 2020.

720 Leblanc, M. J., Tregoning, P., Ramillien, G., Tweed, S. O. and Fakes, A.: Basin-scale, integrated observations of the early 21st
721 century multiyear drought in southeast Australia, *Water Resour. Res.*, 45(4), 1–10, doi:10.1029/2008WR007333, 2009.

722 Lesk, C., Rowhani, P. and Ramankutty, N.: Influence of extreme weather disasters on global crop production, *Nature*, 529(7584),
723 84–87, doi:10.1038/nature16467, 2016.

724 Leuning, R., Kelliher, F. M., Pury, D. G. G. and Schulze, E.-D.: Leaf nitrogen, photosynthesis, conductance and transpiration:
725 scaling from leaves to canopies, *Plant, Cell Environ.*, 18(10), 1183–1200, doi:10.1111/j.1365-3040.1995.tb00628.x, 1995.

726 Marchionni, V., Daly, E., Manoli, G., Tapper, N. J., Walker, J. P. and Fatichi, S.: Groundwater buffers drought effects and
727 climate variability in urban reserves, *Water Resour. Res.*, 56(5), doi:10.1029/2019WR026192, 2020.

728 Martens, B., Miralles, D. G., Lievens, H., van der Schalie, R., de Jeu, R. A. M., Fernández-Prieto, D., Beck, H. E., Dorigo, W.
729 A. and Verhoest, N. E. C. C.: GLEAM v3: satellite-based land evaporation and root-zone soil moisture, *Geosci. Model
730 Dev.*, 10(5), 1903–1925, doi:10.5194/gmd-10-1903-2017, 2017.

731 Martínez-de la Torre, A. and Miguez-Macho, G.: Groundwater influence on soil moisture memory and land–atmosphere fluxes
732 in the Iberian Peninsula, *Hydrol. Earth Syst. Sci.*, 23(12), 4909–4932, doi:10.5194/hess-23-4909-2019, 2019.

733 Martinez, J. A., Dominguez, F. and Miguez-Macho, G.: Effects of a groundwater scheme on the simulation of soil moisture and
734 evapotranspiration over southern South America, *J. Hydrometeorol.*, 17(11), 2941–2957, doi:10.1175/JHM-D-16-0051.1,
735 2016a.

736 Martinez, J. A., Dominguez, F. and Miguez-Macho, G.: Impacts of a groundwater scheme on hydroclimatological conditions
737 over southern South America, *J. Hydrometeorol.*, 17(11), 2959–2978, doi:10.1175/JHM-D-16-0052.1, 2016b.

738 Massmann, A., Gentine, P. and Lin, C.: When does vapor pressure deficit drive or reduce evapotranspiration?, *J. Adv. Model.
739 Earth Syst.*, 11(10), 3305–3320, doi:10.1029/2019MS001790, 2019.

740 Maxwell, R. M., Chow, F. K. and Kollet, S. J.: The groundwater–land-surface–atmosphere connection: Soil moisture effects on
741 the atmospheric boundary layer in fully-coupled simulations, *Adv. Water Resour.*, 30(12), 2447–2466,
742 doi:10.1016/j.advwatres.2007.05.018, 2007.

743 Maxwell, R. M., Lundquist, J. K., Mirocha, J. D., Smith, S. G., Woodward, C. S. and Tompson, A. F. B.: Development of a
744 coupled groundwater–atmosphere model, *Mon. Weather Rev.*, 139(1), 96–116, doi:10.1175/2010MWR3392.1, 2011.

745 McVicar, T. R., Van Niel, T. G., Li, L. T., Roderick, M. L., Rayner, D. P., Ricciardulli, L. and Donohue, R. J.: Wind speed
746 climatology and trends for Australia, 1975–2006: Capturing the stilling phenomenon and comparison with near-surface
747 reanalysis output, *Geophys. Res. Lett.*, 35(20), 1–6, doi:10.1029/2008GL035627, 2008.

748 Medlyn, B. E., Duursma, R. A., Eamus, D., Ellsworth, D. S., Prentice, C. I., Barton, C. V. M., Crous, K. Y., De Angelis, P.,
749 Freeman, M. and Wingate, L.: Reconciling the optimal and empirical approaches to modelling stomatal conductance, *Glob.*
750 *Chang. Biol.*, 17(6), 2134–2144, doi:10.1111/j.1365-2486.2010.02375.x, 2011.

751 Mercado, L. M., Medlyn, B. E., Huntingford, C., Oliver, R. J., Clark, D. B., Sitch, S., Zelazowski, P., Kattge, J., Harper, A. B.
752 and Cox, P. M.: Large sensitivity in land carbon storage due to geographical and temporal variation in the thermal response
753 of photosynthetic capacity, *New Phytol.*, 218(4), 1462–1477, doi:10.1111/nph.15100, 2018.

754 Miller, G. R., Chen, X., Rubin, Y., Ma, S. and Baldocchi, D. D.: Groundwater uptake by woody vegetation in a semiarid oak
755 savanna, *Water Resour. Res.*, 46(10), 2009WR008902, doi:10.1029/2009WR008902, 2010.

756 Miralles, D. G., Holmes, T. R. H. H., De Jeu, R. A. M. M., Gash, J. H., Meesters, A. G. C. A. C. A. and Dolman, A. J.: Global
757 land-surface evaporation estimated from satellite-based observations, *Hydrol. Earth Syst. Sci.*, 15(2), 453–469,
758 doi:10.5194/hess-15-453-2011, 2011.

759 Miralles, D. G., Teuling, A. J., van Heerwaarden, C. C. and Vilà-Guerau de Arellano, J.: Mega-heatwave temperatures due to
760 combined soil desiccation and atmospheric heat accumulation, *Nat. Geosci.*, 7(5), 345–349, doi:10.1038/ngeo2141, 2014.

761 Miralles, D. G., Gentine, P., Seneviratne, S. I. and Teuling, A. J.: Land-atmospheric feedbacks during droughts and heatwaves:
762 state of the science and current challenges, *Ann. N. Y. Acad. Sci.*, 1436(1), 19–35, doi:10.1111/nyas.13912, 2019.

763 Mitchell, P. J., O’Grady, A. P., Hayes, K. R. and Pinkard, E. A.: Exposure of trees to drought-induced die-off is defined by a
764 common climatic threshold across different vegetation types, *Ecol. Evol.*, 4(7), 1088–1101, doi:10.1002/ece3.1008, 2014.

765 Mu, M.: bibivking/Groundwater_Vegetation_Heatwave_Drought: Groundwater Vegetation Heatwave Drought (v1.0), Zenodo,
766 <https://doi.org/10.5281/zenodo.5158498>, 2021.

767 Mu, M., De Kauwe, M. G., Ukkola, A. M., Pitman, A. J., Gimeno, T. E., Medlyn, B. E., Or, D., Yang, J. and Ellsworth, D. S.:
768 Evaluating a land surface model at a water-limited site: implications for land surface contributions to droughts and
769 heatwaves, *Hydrol. Earth Syst. Sci.*, 25(1), 447–471, doi:10.5194/hess-25-447-2021, 2021.

770 Mukherjee, S., Ashfaq, M. and Mishra, A. K.: Compound Drought and Heatwaves at a Global Scale: The role of natural climate
771 variability-associated synoptic patterns and land-surface energy budget anomalies, *J. Geophys. Res. Atmos.*, 125(11),
772 doi:10.1029/2019JD031943, 2020.

773 Nairn, J. R. and Fawcett, R. J. B.: The excess heat factor: A metric for heatwave intensity and its use in classifying heatwave
774 severity, *Int. J. Environ. Res. Public Health*, 12(1), 227–253, doi:10.3390/ijerph120100227, 2014.

775 National Climate Centre: The exceptional January–February 2009 heatwave in south-eastern Australia. [online] Available from:
776 <http://www.bom.gov.au/climate/current/statements/scs17c.pdf>, 2009.

777 NCI: CABLE: The Community Atmosphere Biosphere Land Exchange Model, available at: <https://trac.nci.org.au/trac/cable>,
778 last access: 4 August 2021.

779 O'sullivan, O. S., Heskel, M. A., Reich, P. B., Tjoelker, M. G., Weerasinghe, L. K., Penillard, A., Zhu, L., Egerton, J. J. G.,
780 Bloomfield, K. J., Creek, D. and others: Thermal limits of leaf metabolism across biomes, *Glob. Chang. Biol.*, 23(1), 209–
781 223, 2017.

782 Orth, R. and Destouni, G.: Drought reduces blue-water fluxes more strongly than green-water fluxes in Europe, *Nat. Commun.*,
783 9(1), 3602, doi:10.1038/s41467-018-06013-7, 2018.

784 Perkins-Kirkpatrick, S. E., White, C. J., Alexander, L. V., Argüeso, D., Boschat, G., Cowan, T., Evans, J. P., Ekström, M., Oliver,
785 E. C. J., Phatak, A. and Purich, A.: Natural hazards in Australia: heatwaves, *Clim. Change*, 139(1), 101–114,
786 doi:10.1007/s10584-016-1650-0, 2016.

787 Perkins, S. E.: A review on the scientific understanding of heatwaves—Their measurement, driving mechanisms, and changes
788 at the global scale, *Atmos. Res.*, 164–165, 242–267, doi:10.1016/j.atmosres.2015.05.014, 2015.

789 Raupach, M. R.: Simplified expressions for vegetation roughness length and zero-plane displacement as functions of canopy
790 height and area index, *Boundary-Layer Meteorol.*, 71(1–2), 211–216, doi:10.1007/BF00709229, 1994.

791 Raupach, M. R., Finkele, K. and Zhang, L.: SCAM: a soil-canopy-atmosphere model: description and comparisons with field
792 data, CSIRO Centre for Environmental Mechanics, Canberra, Australia, <https://doi.org/10.4225/08/5a30195883b8f>, 1997.

793 Raupach, M. R., Haverd, V. and Briggs, P. R.: Sensitivities of the Australian terrestrial water and carbon balances to climate
794 change and variability, *Agric. For. Meteorol.*, 182–183, 277–291, doi:10.1016/j.agrformet.2013.06.017, 2013.

795 Richards, J. H. and Caldwell, M. M.: Hydraulic lift: Substantial nocturnal water transport between soil layers by *Artemisia*
796 *tridentata* roots, *Oecologia*, 73(4), 486–489, doi:10.1007/BF00379405, 1987.

797 Ruehr, N. K., Grote, R., Mayr, S. and Arneth, A.: Beyond the extreme: recovery of carbon and water relations in woody plants
798 following heat and drought stress, *Tree Physiol.*, 39(8), 1285–1299, doi:10.1093/treephys/tpz032, 2019.

799 Sandi, S. G., Rodriguez, J. F., Saintilan, N., Wen, L., Kuczera, G., Riccardi, G. and Saco, P. M.: Resilience to drought of dryland
800 wetlands threatened by climate change, *Sci. Rep.*, 10(1), 13232, doi:10.1038/s41598-020-70087-x, 2020.

801 Schenk, H. J. and Jackson, R. B.: The global biogeography of roots, *Ecol. Monogr.*, 72(3), 311–328,
802 doi:[https://doi.org/10.1890/0012-9615\(2002\)072\[0311:TGBOR\]2.0.CO;2](https://doi.org/10.1890/0012-9615(2002)072[0311:TGBOR]2.0.CO;2), 2002.

803 Schumacher, D. L., Keune, J., van Heerwaarden, C. C., Vilà-Guerau de Arellano, J., Teuling, A. J. and Miralles, D. G.:
804 Amplification of mega-heatwaves through heat torrents fuelled by upwind drought, *Nat. Geosci.*, 12(9), 712–717,
805 doi:10.1038/s41561-019-0431-6, 2019.

806 Seneviratne, S. I., Corti, T., Davin, E. L., Hirschi, M., Jaeger, E. B., Lehner, I., Orlowsky, B. and Teuling, A. J.: Investigating
807 soil moisture–climate interactions in a changing climate: A review, *Earth-Science Rev.*, 99(3–4), 125–161,
808 doi:10.1016/j.earscirev.2010.02.004, 2010.

809 Shrestha, P., Sulis, M., Masbou, M., Kollet, S. and Simmer, C.: A scale-consistent terrestrial systems modeling platform based
810 on COSMO, CLM, and ParFlow, *Mon. Weather Rev.*, 142(9), 3466–3483, doi:10.1175/MWR-D-14-00029.1, 2014.

811 Smith, N. G. and Dukes, J. S.: Plant respiration and photosynthesis in global-scale models: incorporating acclimation to
812 temperature and CO₂, *Glob. Chang. Biol.*, 19(1), 45–63, doi:10.1111/j.1365-2486.2012.02797.x, 2013.

813 Smith, N. G., Malyshev, S. L., Shevliakova, E., Kattge, J. and Dukes, J. S.: Foliar temperature acclimation reduces simulated
814 carbon sensitivity to climate, *Nat. Clim. Chang.*, 6(4), 407–411, doi:10.1038/nclimate2878, 2016.

815 Swenson, S. C. and Lawrence, D. M.: Assessing a dry surface layer-based soil resistance parameterization for the Community
816 Land Model using GRACE and FLUXNET-MTE data, *J. Geophys. Res. Atmos.*, 119(17), 10,299-10,312,
817 doi:10.1002/2014JD022314, 2014.

818 Teuling, A. J., Van Loon, A. F., Seneviratne, S. I., Lehner, I., Aubinet, M., Heinesch, B., Bernhofer, C., Grünwald, T., Prasse,
819 H. and Spank, U.: Evapotranspiration amplifies European summer drought, *Geophys. Res. Lett.*, 40(10), 2071–2075,
820 doi:10.1002/grl.50495, 2013.

821 Thorburn, P. J., Walker, G. R. and Woods, P. H.: Comparison of diffuse discharge from shallow water tables in soils and salt
822 flats, *J. Hydrol.*, 136(1–4), 253–274, doi:10.1016/0022-1694(92)90014-M, 1992.

823 Trudinger, C. M., Haverd, V., Briggs, P. R. and Canadell, J. G.: Interannual variability in Australia's terrestrial carbon cycle
824 constrained by multiple observation types, *Biogeosciences*, 13(23), 6363–6383, doi:10.5194/bg-13-6363-2016, 2016.

825 Trugman, A. T., Medvigy, D., Mankin, J. S. and Anderegg, W. R. L. L.: Soil moisture stress as a major driver of carbon cycle
826 uncertainty, *Geophys. Res. Lett.*, 45(13), 6495–6503, doi:10.1029/2018GL078131, 2018.

827 Ukkola, A. M., De Kauwe, M. G., Pitman, A. J., Best, M. J., Abramowitz, G., Haverd, V., Decker, M. and Haughton, N.: Land
828 surface models systematically overestimate the intensity, duration and magnitude of seasonal-scale evaporative droughts,
829 *Environ. Res. Lett.*, 11(10), 104012, doi:10.1088/1748-9326/11/10/104012, 2016a.

830 Ukkola, A. M., Pitman, A. J., Decker, M., De Kauwe, M. G., Abramowitz, G., Kala, J. and Wang, Y.-P.: Modelling
831 evapotranspiration during precipitation deficits: identifying critical processes in a land surface model, *Hydrol. Earth Syst.
832 Sci.*, 20(6), 2403–2419, doi:10.5194/hess-20-2403-2016, 2016b.

833 Ukkola, A. M., De Kauwe, M. G., Roderick, M. L., Abramowitz, G. and Pitman, A. J.: Robust future changes in meteorological
834 drought in CMIP6 projections despite uncertainty in precipitation, *Geophys. Res. Lett.*, 47(11), e2020GL087820,
835 doi:10.1029/2020GL087820, 2020.

836 Verdon-Kidd, D. C. and Kiem, A. S.: Nature and causes of protracted droughts in southeast Australia: Comparison between the
837 Federation, WWII, and Big Dry droughts, *Geophys. Res. Lett.*, 36(22), L22707, doi:10.1029/2009GL041067, 2009.

838 Wada, Y.: Impacts of groundwater pumping on regional and global water resources, in: *Terrestrial Water Cycle and Climate
839 Change*, American Geophysical Union, edited by: Tang, Q. and Oki, T., Hoboken, United States, 71–101, doi:
840 10.1002/9781118971772.ch5, 2016.

841 Wan Z.: MOD11A1 MODIS/Terra Land Surface Temperature and the Emissivity Daily L3 Global 1km SIN Grid, NASA LP
842 DAAC, <http://doi.org/10.5067/MODIS/MOD11A1.006>, 2015a. Last access: 14 April 2021.

843 Wan Z.: MYD11A1 MODIS/Aqua Land Surface Temperature and the Emissivity Daily L3 Global 1km SIN Grid, NASA LP
844 DAAC, <http://doi.org/10.5067/MODIS/MYD11A1.006>, 2015b. Last access: 14 April 2021.

845 Wan, Z. and Li, Z.-L.: A physics-based algorithm for retrieving land-surface emissivity and temperature from EOS/MODIS
846 data, *IEEE Trans. Geosci. Remote Sens.*, 35(4), 980–996, doi:10.1109/36.602541, 1997.

847 Wang, K. and Dickinson, R. E.: A review of global terrestrial evapotranspiration: Observation, modeling, climatology, and
848 climatic variability, *Rev. Geophys.*, 50(2), doi:10.1029/2011RG000373, 2012.

849 Wang, P., Niu, G., Fang, Y., Wu, R., Yu, J., Yuan, G., Pozdniakov, S. P. and Scott, R. L.: Implementing dynamic root
850 optimization in Noah-MP for simulating phreatophytic root water uptake, *Water Resour. Res.*, 54(3), 1560–1575,
851 doi:10.1002/2017WR021061, 2018.

852 Wang, Y.-P. and Leuning, R.: A two-leaf model for canopy conductance, photosynthesis and partitioning of available energy I:
853 Model description and comparison with a multi-layered model, *Agric. For. Meteorol.*, 91(1–2), 89–111,
854 doi:10.1016/S0168-1923(98)00061-6, 1998.

855 Wang, Y. P., Kowalczyk, E., Leuning, R., Abramowitz, G., Raupach, M. R., Pak, B., van Gorsel, E. and Luhar, A.: Diagnosing
856 errors in a land surface model (CABLE) in the time and frequency domains, *J. Geophys. Res.*, 116(G1), G01034,
857 doi:10.1029/2010JG001385, 2011.

858 Warren, J. M., Hanson, P. J., Iversen, C. M., Kumar, J., Walker, A. P. and Wullschleger, S. D.: Root structural and functional
859 dynamics in terrestrial biosphere models - evaluation and recommendations, *New Phytol.*, 205(1), 59–78,
860 doi:10.1111/nph.13034, 2015.

861 Watkins, M. M., Wiese, D. N., Yuan, D.-N., Boening, C. and Landerer, F. W.: Improved methods for observing Earth's time
862 variable mass distribution with GRACE using spherical cap mascons, *J. Geophys. Res. Solid Earth*, 120(4), 2648–2671,
863 doi:10.1002/2014JB011547, 2015.

864 Wiese, D. N., Landerer, F. W. and Watkins, M. M.: Quantifying and reducing leakage errors in the JPL RL05M GRACE mascon
865 solution, *Water Resour. Res.*, 52(9), 7490–7502, doi:10.1002/2016WR019344, 2016.

866 Wiese, D. N., Yuan, D.-N., Boening, C., Landerer, F. W., Watkins, M. M.: JPL GRACE Mascon Ocean, Ice, and Hydrology
867 Equivalent Water Height Release 06 Coastal Resolution Improvement (CRI) Filtered Version 1.0. Ver. 1.0., PO.DAAC,
868 CA, USA. <http://dx.doi.org/10.5067/TEMSC-3MJC6>, 2018. Last access: 14 April 2021.

869 Yang, J., Duursma, R. A., De Kauwe, M. G., Kumarathunge, D., Jiang, M., Mahmud, K., Gimeno, T. E., Crous, K. Y., Ellsworth,
870 D. S., Peters, J., Choat, B., Eamus, D. and Medlyn, B. E.: Incorporating non-stomatal limitation improves the performance
871 of leaf and canopy models at high vapour pressure deficit, *Tree Physiol.*, 39(12), 1961–1974, doi:10.1093/treephys/tpz103,
872 2019.

873 Zencich, S. J., Froend, R. H., Turner, J. V. and Gailitis, V.: Influence of groundwater depth on the seasonal sources of water
874 accessed by Banksia tree species on a shallow, sandy coastal aquifer, *Oecologia*, 131(1), 8–19, doi:10.1007/s00442-001-
875 0855-7, 2002.

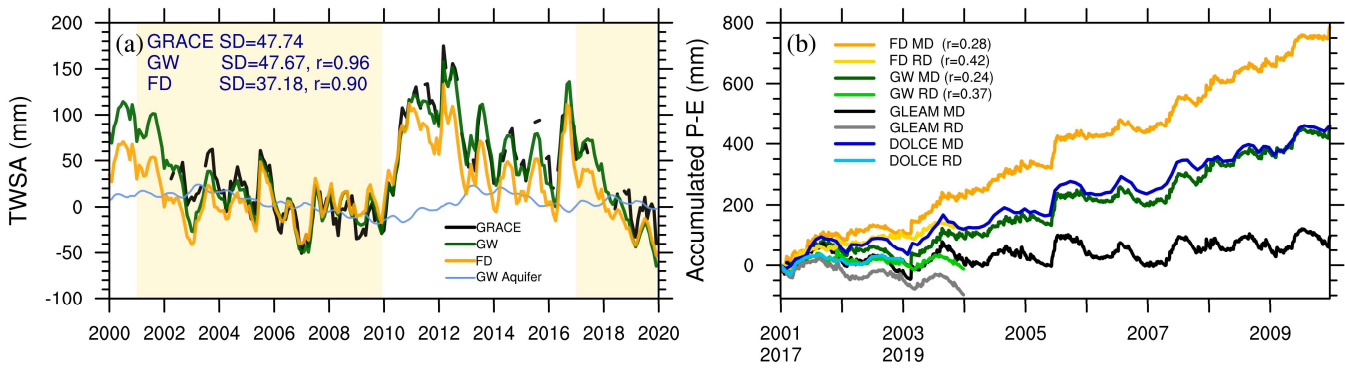
876 Zeng, X. and Decker, M.: Improving the numerical solution of soil moisture–based Richards equation for land models with a
877 deep or shallow water table, *J. Hydrometeorol.*, 10(1), 308–319, doi:10.1175/2008JHM1011.1, 2009.

878 Zhang, H., Pak, B., Wang, Y. P., Zhou, X., Zhang, Y. and Zhang, L.: Evaluating surface water cycle simulated by the Australian
879 Community Land Surface Model (CABLE) across Different Spatial and Temporal Domains, *J. Hydrometeorol.*, 14(4),
880 1119–1138, doi:10.1175/JHM-D-12-0123.1, 2013.

881 Zhou, S., Williams, A. P., Berg, A. M., Cook, B. I., Zhang, Y., Hagemann, S., Lorenz, R., Seneviratne, S. I. and Gentine, P.:
882 Land–atmosphere feedbacks exacerbate concurrent soil drought and atmospheric aridity, *Proc. Natl. Acad. Sci.*, 116(38),
883 18848–18853, doi:10.1073/pnas.1904955116, 2019.

884 Zipper, S. C., Keune, J. and Kollet, S. J.: Land use change impacts on European heat and drought: remote land-atmosphere
885 feedbacks mitigated locally by shallow groundwater, *Environ. Res. Lett.*, 14(4), 044012, doi:10.1088/1748-9326/ab0db3,
886 2019.

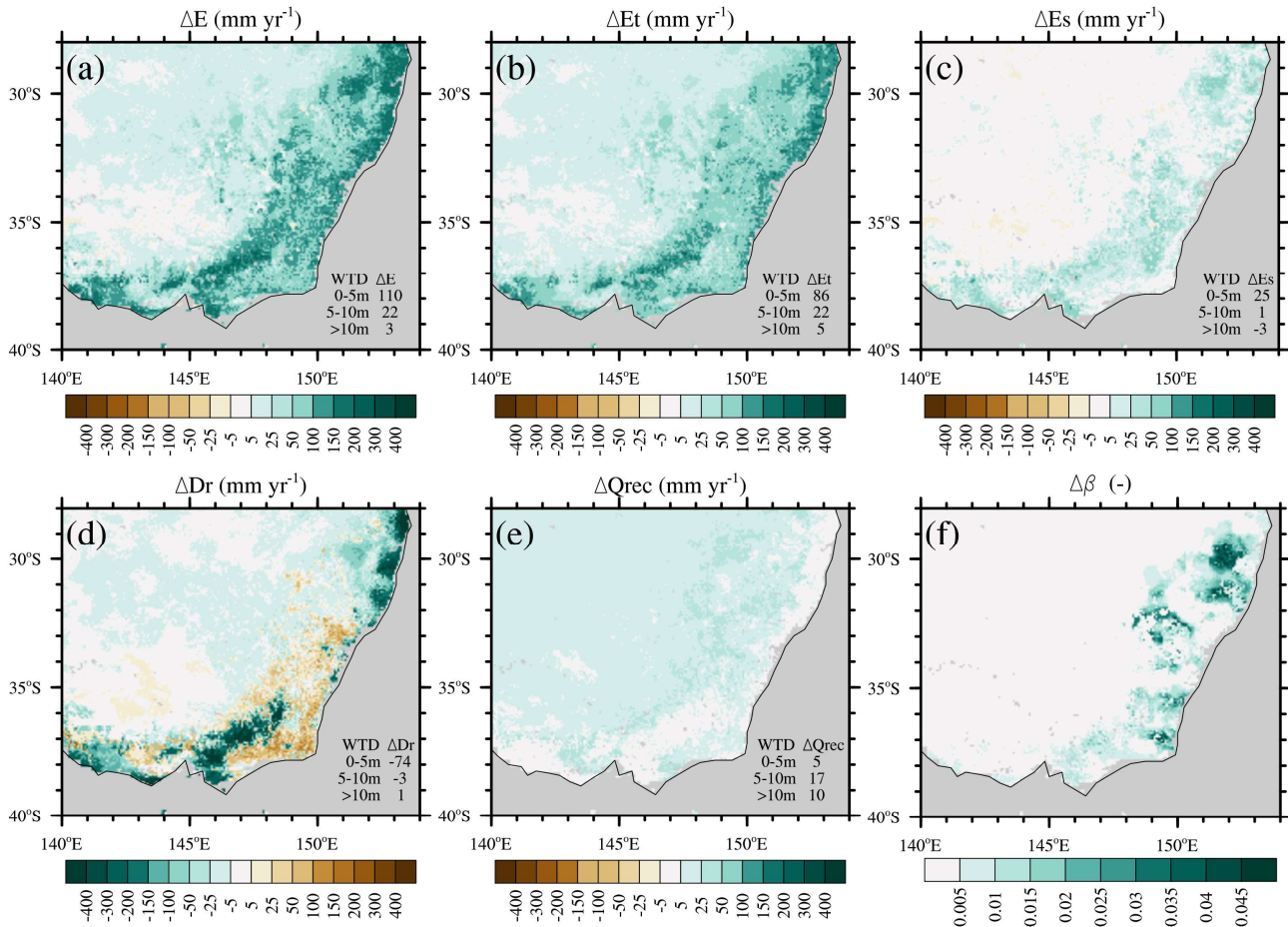
887



888
889
890
891
892
893
894
895

Figure 1 (a) Total water storage anomaly (TWSA) during 2000–2019 and (b) accumulated P–E for the two droughts over S.E. Australia. In panel (a), observations from GRACE are shown in black, the GW simulation in green, FD in orange and the aquifer water storage anomaly in GW in blue. The shading in panel (a) highlights the two drought periods. The left top corner of panel (a) displays the correlation (r) between GRACE and GW/FD, as well as the standard deviation (SD, mm) of GRACE, GW and FD over the periods when GRACE and the simulations coincide. Panel (b) shows the accumulated P–E for two periods; the dark lines show the 2001–2009 Millennium drought (MD) and the light lines show the 2017–2019 recent drought (RD). The correlation (r) between the P and E is shown in the legend of panel (b).

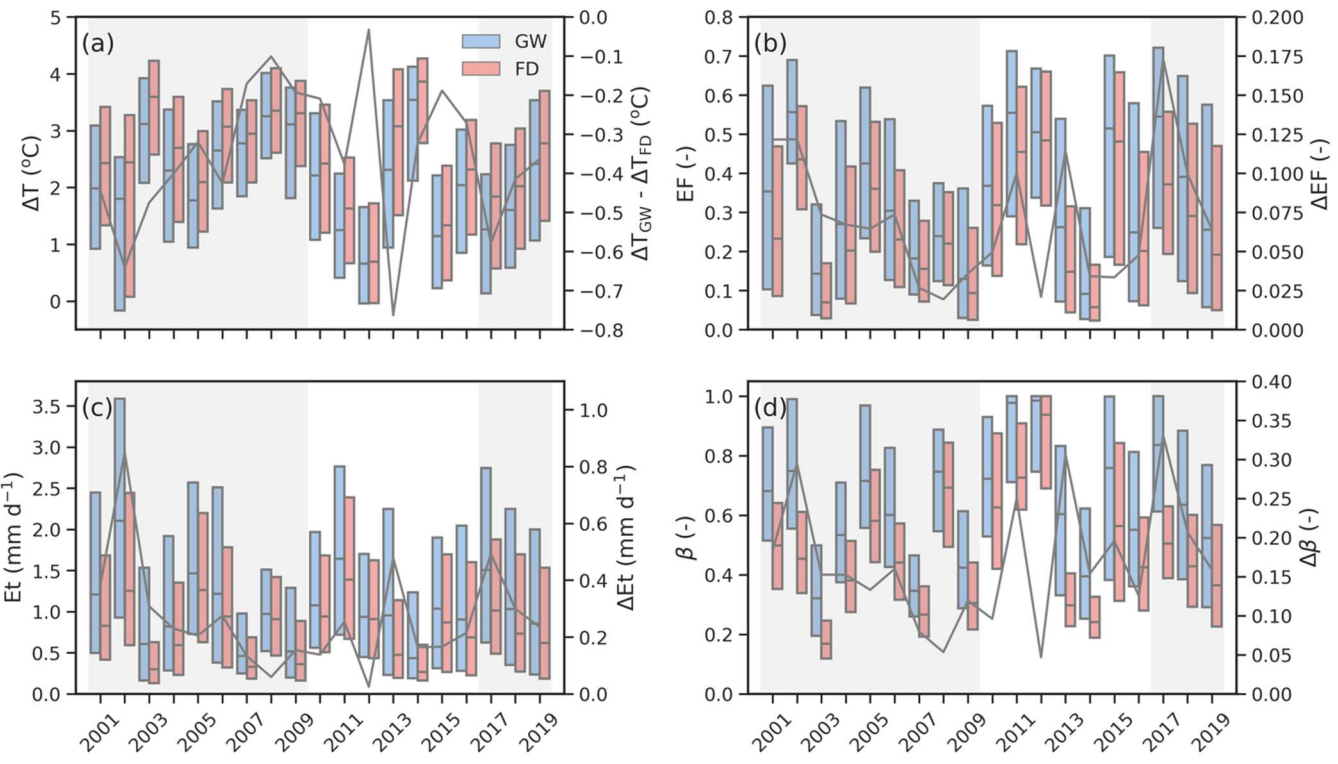
896



897
898

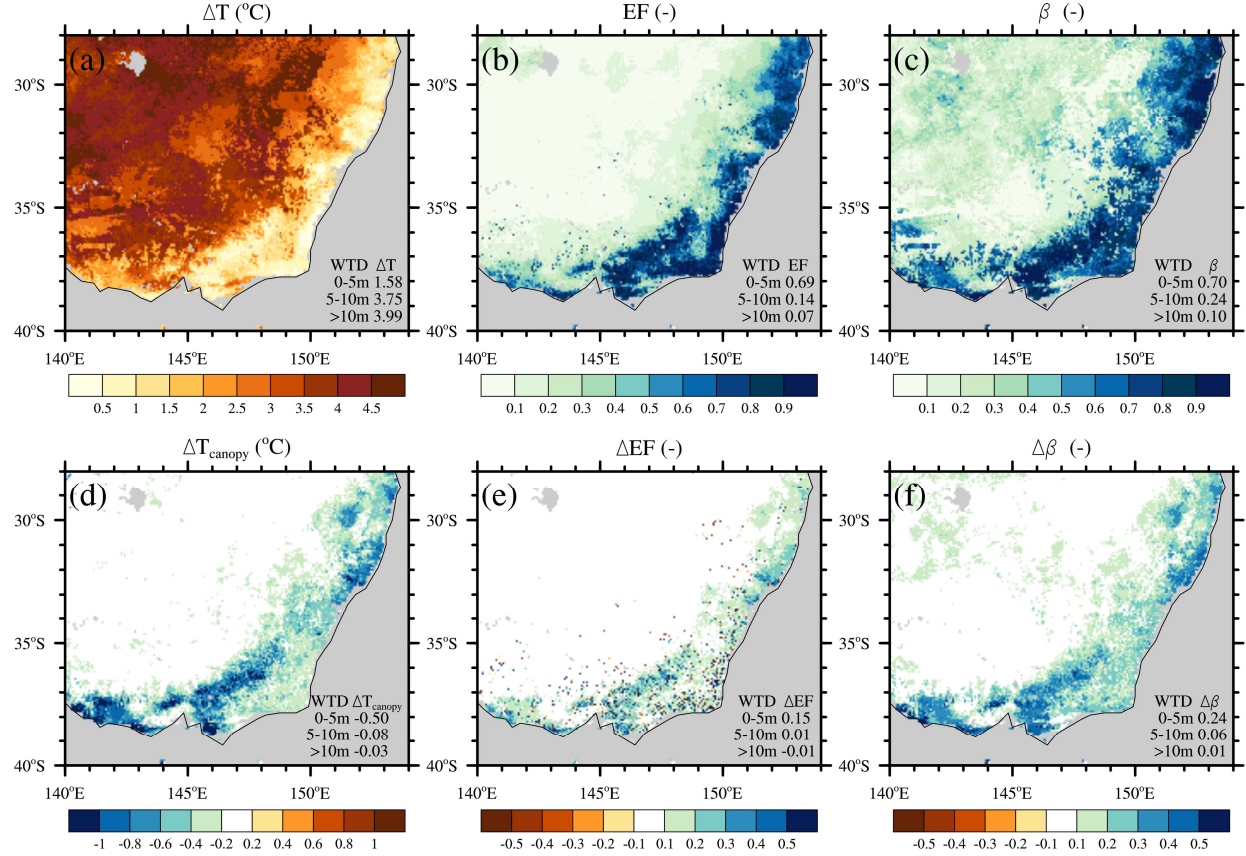
Figure 2. The overall influence of groundwater during the recent drought. (a)–(e) are the difference (GW–FD) in evapotranspiration (ΔE), transpiration (ΔE_t), soil evaporation (ΔE_s), vertical drainage (ΔD_r) and recharge from the aquifer to soil column (ΔQ_{rec}), respectively. In the bottom right of panels (a)–(e), the average of each variable over selected water table depths (WTD) is provided. (f) is the maximum night-time water stress factor difference ($\Delta\beta$) between 3 am (i.e. predawn when the soil is relatively moist following capillary lift overnight) and 9 pm the previous day. We only include rainless nights in January 2019 to calculate $\Delta\beta$ to remove any influence of overnight rainfall.

904

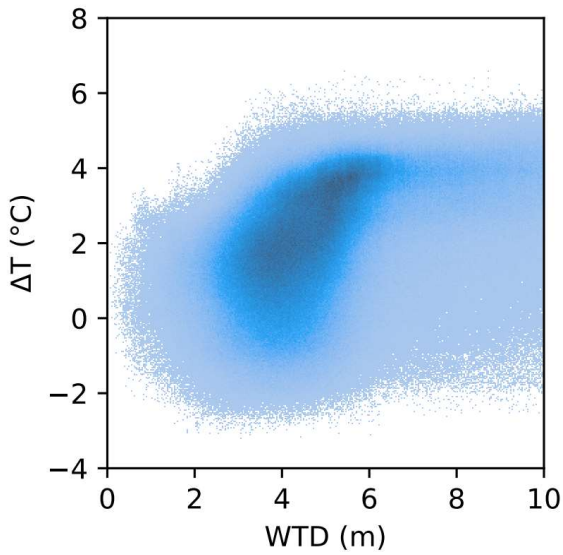


905
906 **Figure 3.** Groundwater-induced differences in (a) $T_{\text{canopy}} - T_{\text{air}}$ (ΔT), (b) evaporative fraction (EF),
907 (c) transpiration (Et), and (d) water stress
908 factor (β) during 2000-2019 summer heatwaves over forested areas (the green region in Figure S2a). The left y-axis is the scale for boxes.
909 The blue boxes refer to the GW experiment and the red boxes to FD. For each box, the middle line is the median, the upper border is the 75th
910 percentile, and the lower border is 25th percentile. The right y-axis is the scale for the grey lines which display the difference in the medians
(GW-FD). The shadings highlight the two drought periods.

911



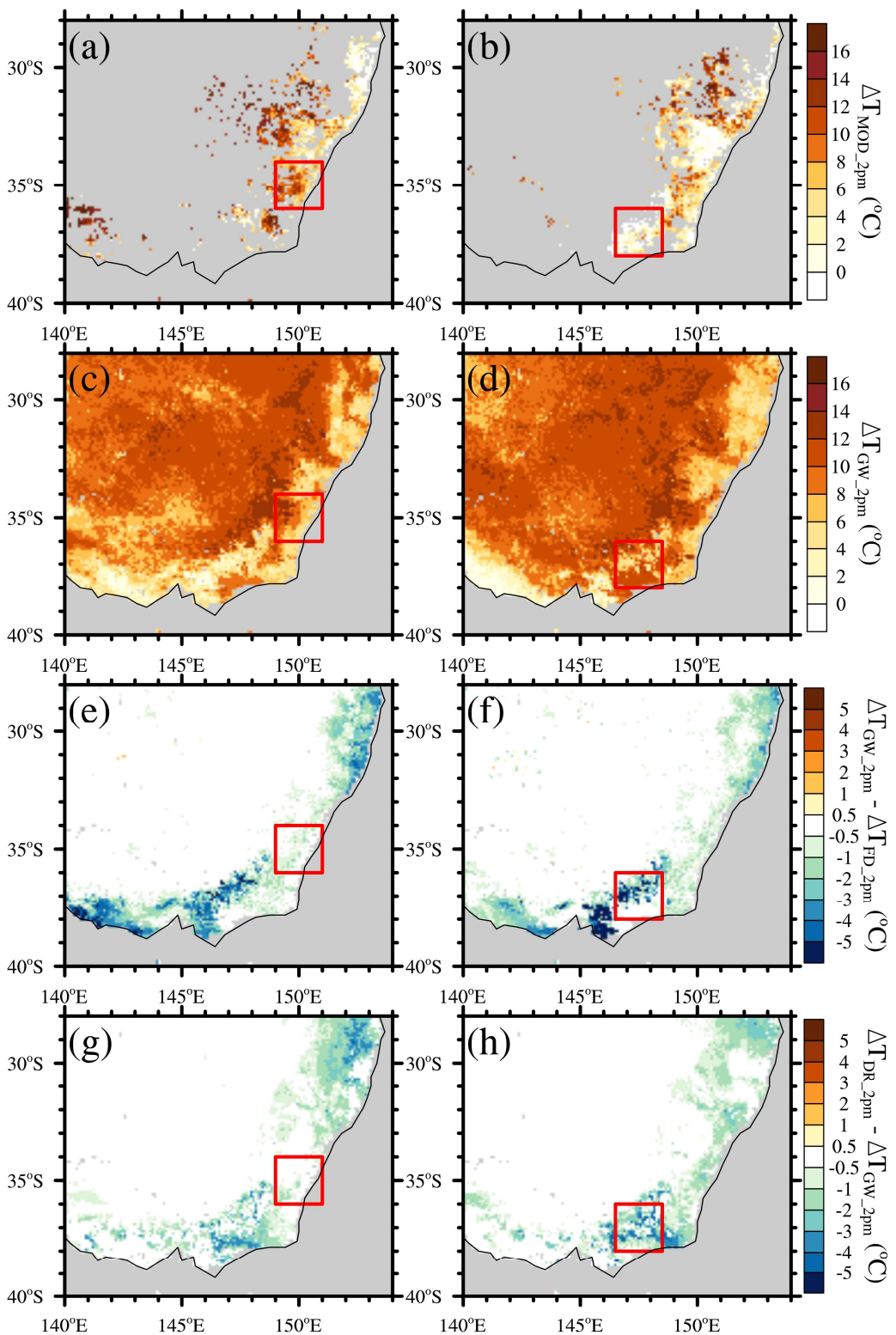
912
913 **Figure 4.** Land response to heatwaves during the recent drought. Panels (a)-(c) are the mean $T_{\text{canopy}} - T_{\text{air}}$ (ΔT),
914 evaporative fraction (EF), and soil water stress factor (β) in GW, respectively, during 2017-2019 summer heatwaves. Panel (d)-(f) are the difference (GW-FD) of T_{canopy} , EF
915 and β . In the bottom right of each plot, the average of each variable over selected water table depths (WTD) is provided.
916 Note that the colour bar is switched between (d) and (e)-(f).



917

918

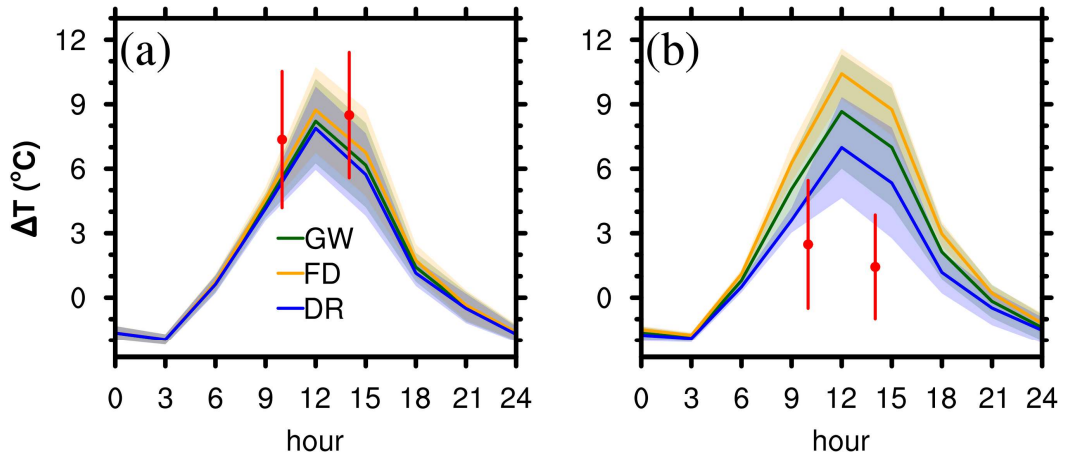
919 **Figure 5.** A density scatter plot of $T_{\text{canopy}} - T_{\text{air}}$ (ΔT) versus water table depth (WTD) in GW simulations over forested areas in all heatwaves
920 during 2000–2019. Every tree pixel on each heatwave day accounts for one record and the darker colours show higher recorded densities.



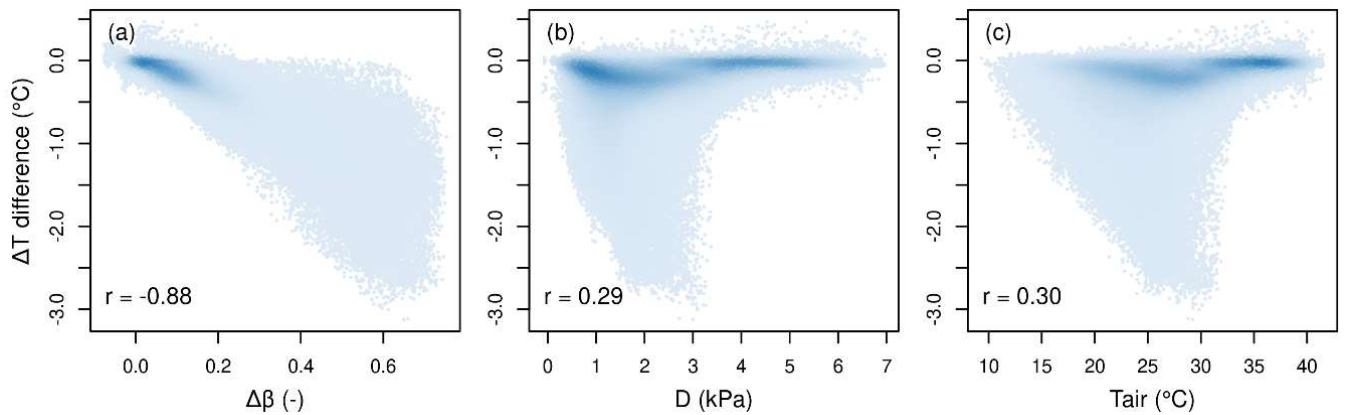
921
922
923 **Figure 6.** The simulation of two heatwaves on 15th (left column) and 25th January 2019 (right column). The first row shows the difference
924 between MODIS land surface temperature (LST) and T_{air} at 2 pm (ΔT_{MOD_2pm}) (only forested areas with good LST quality data are displayed).
925 The second row is the GW simulation of ΔT at 2 pm (ΔT_{GW_2pm}). The third row is the difference of ΔT at 2 pm between GW and FD simulations
926 ($\Delta T_{GW_2pm} - \Delta T_{FD_2pm}$). The last row is the same as the third row but for the difference between the DR and GW simulations ($\Delta T_{DR_2pm} -$
927 ΔT_{GW_2pm}). Note that the comparsion between GW/FD/DR and MODIS LST is shown in Figure S7.

928

929



930
931
932 **Figure 7.** Diurnal cycle of ΔT on 15th (left column) and 25th January 2019 (right column) over the selected regions shown in Figure 6. The
933 shadings show the uncertainty in every simulation defined as one standard deviation (SD) among the selected pixels.
934 The red dots are MODIS LST minus T_{air} with the uncertainty shown by the red error bars. For both regions, only pixels available in MODIS are shown.



935
936
937
938
939
940 **Figure 8.** Density scatter plots showing the three factors that influence the difference in $T_{canopy}-T_{air}$ between GW and FD (ΔT , expressed as
941 GW-FD difference). (a) is ΔT difference against the β difference (GW-FD) ($\Delta\beta$), (b) is ΔT difference against vapour pressure deficit (D), and
942 (c) is ΔT difference against T_{air} . Each point corresponds to a tree pixel on a heatwave day in January 2019. The darker colours illustrate where
943 the records are more dense. The correlation (r) between the x- and y-axis is shown in the bottom left of each panel.